Acrylates-based hydrophilic co-polymeric nanobeads as nanocarriers for imaging agents

Sara Cerra [a,*], Valentina Dini [b,c], Tommaso A. Salamone [a], Farid Hajareh Haghighi [a], Martina Mercurio [a], Antonella Cartoni [a], Alessandra Del Giudice [a], Martina Marsotto [d], Iole Venditti [d], Chiara Battocchio [d], Francesca A. Scaramuzzo [e], Roberto Matassa [f], Stefania Nottola [f], Riccardo Faccini [g,c], Riccardo Mirabelli [h,c], Ilaria Fratoddi [a,*]

[a] Department of Chemistry, Sapienza University of Rome, P.le A. Moro 5, 00185 Rome, Italy
[b] National Center for Innovative Technologies in Public Health, Istituto Superiore di Sanità, Viale Regina Elena 299, 00161 Rome, Italy
[c] INFN, sezione di Roma 1, P.le Aldo Moro 5, 00185 Rome, Italy
[d] Department of Sciences, Roma Tre University, Via della Vasca Navale 79, 00146 Rome, Italy
[e] Department of Basic and Applied Sciences for Engineering (SBAI), Sapienza University of Rome, Via A. Scarpa 14, 00161 Rome, Italy
[f] Department of Anatomical, Histological, Forensic and Orthopaedic Sciences, Section of Human Anatomy, Sapienza University of Rome, Via A. Borelli 50, 00161 Rome, Italy
[g] Department of Physics, Sapienza University of Rome, P.le A. Moro 5, 00185 Rome, Italy
[h] Department of Chemistry and Technologies of Drug, Sapienza University of Rome, P.le A. Moro 5, 00185 Rome, Italy

HIGHLIGHTS

- Acrylates-based polymeric nanobeads are synthesized *via* surfactant-free radical emulsion polymerization.
- Structure and morphology are evaluated by different characterization techniques.
- Surface Y3 + (aq) ions loading and release is studied.
- In situ FITC dye is encapsulated inside nanoparticles core to obtain fluorescent nanoparticles.
- The *in vitro* studies on T98G cells show absence of cytotoxicity within 24 h.

GRAPHICAL ABSTRACT
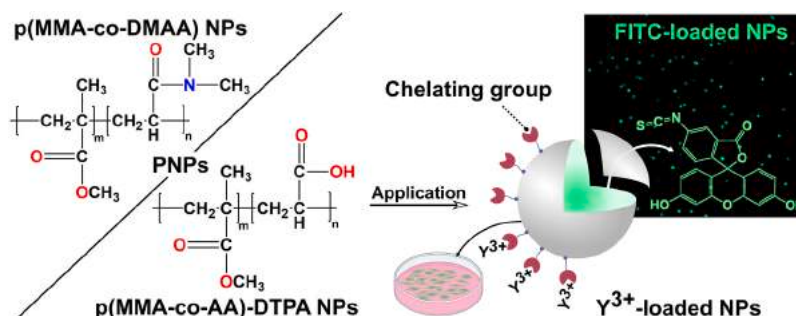
ARTICLE INFO

ABSTRACT

Acrylates-based co-polymeric nanoparticles (PNPs) are widely used in nanomedicine applications due to their tunable hydrophilic surface, physical and chemical versatility. Particularly attracting is their use as nanocarriers for imaging agents. Herein, methyl methacrylate (MMA) and *N,N*-dimethylacrylamide (DMAA) monomers were used to synthesize hydrophilic p(MMA-co-DMAA) nanoparticles in the 200–600 nm size range *via* surfactant-free radical emulsion polymerization technique. Different MMA/DMAA molar ratios, temperatures, and reaction times were investigated to evaluate their role in determining the average particle size, polydispersity, and optimizing surface properties of PNPs. Nanoparticles formation, stability (in water and culture medium for cell growth), swelling behavior, structural features and molecular weights were assessed by spectroscopic, non-

* Corresponding authors.
  E-mail addresses: sara.cerra@uniroma1.it (S. Cerra), ilaria.fratoddi@uniroma1.it (I. Fratoddi).

spectroscopic, and chromatographic techniques. Morphological profiles confirming spherical-shaped NPs were obtained at solid state *via* microscopies (FESEM, AFM). To use such colloids as potential imaging agents, PNPs were loaded with $Y^{3+}_{(aq)}$ ions by the addition of aqueous solutions of YCl_3 at different concentrations, and results compared with p(MMA-co-AA)-DTPA NPs (AA = acrylic acid) functionalized with DTPA chelating agent. Yttrium ions loading percentage was *ca.* 90% for both p(MMA-co-DMAA) and p(MMA-co-AA)-DTPA, with negligible release (<15%) over a month. Parallelly, optical imaging nanoprobes were obtained by physical encapsulation of fluorescein isothiocyanate isomer I (FITC) dye during the synthesis process, and the spontaneous FITC incorporation was evaluated by spectroscopic studies and fluorescence microscopy. Cytotoxicity studies on pristine and yttrium-loaded nanoparticles were done *in vitro* on human glioblastoma T98G cell line within 24 h of treatment. Transmission electron microscopy (TEM) studies on cancer cells treated with NPs confirmed an active uptake of PNPs through multiple endocytic pathways to reach the perinuclear region of the cell. Overall, this work elucidated the role of synthetic parameters for a rational design of hydrophilic PNPs as nanocarriers for imaging agents with potential applications in theranostics.

1. Introduction

Polymeric nanomaterials have been widely studied and applied in nanomedicine as multifunctional nanoplatforms for diagnostic, monitoring, and therapeutic purposes [1,2]. Nano-based cancer therapy has been developed significantly during the past decades due to the development of biocompatible nanoparticles as suitable drug delivery vehicles to improve the solubility, permeation, and half-life of drugs [3–5]. Among them, polymeric nanoparticles (PNPs) have shown high biocompatibility, chemical stability, permeability, low cost, and low toxicity for the delivery of many drugs [6–8]. Interest in nanostructured co-polymers also arises from the possibility of tailoring the surface of NPs with different functional groups, opening to peculiar (i) surface chemistry and (ii) physicochemical properties [9].

Acrylates-based PNPs with tailored features can be obtained *via* different polymerization techniques, typically in the presence of different surfactant molecules (*e.g.*, sodium dodecyl sulfate, polaxamines, polysorbates, gemini surfactants). When used above the critical micelle concentration (CMC), surfactants allow to obtain NPs with reduced particle size while increasing the particle number concentration [10]. However, the presence of surfactants could lead to aggregation phenomena that impact polydispersity of colloids and release profiles [8]. Moreover, their residual presence could have a negative impact for biomedical applications [11]. Surfactant-free radical emulsion polymerization synthesis represents the most suitable one which can be carried out in aqueous environment [12,13]. Indeed, for the targeting and development of novel agents for diagnostic and therapeutic purposes, it is recommended to follow those synthetic methods which provide narrow-sized NPs with limited-to-no content of contaminants and surfactants. Thus, for biomedical purposes surfactant-free non-biodegradable co-polymeric nanoparticles in which methyl methacrylate represents the main co-monomer are the subject of vast research. For example, S. Jaiswal et al. [14] synthesized chitosan-modified methyl methacrylate polymeric nanoparticles *via* ionic gelation for drug and gene delivery. A. Abdollahi and co-workers [15] obtained functionalized latex nanoparticles *via* emulsion co-polymerization of polystyrene and poly(methyl methacrylate) with potential applications in drug-delivery, bioimaging, cell-labeling, and chemosensors. M. Jahanbakhshi et al. [16] prepared cross-linked poly(vinyl alcohol-co-methyl methacrylate) colloidal nanoparticles as a promising cancer drug delivery system. However, the important aspect is to consider polymer composition, surface charge, core properties, hydrophilicity/lipophilicity, and particle size [17,18].

As reported in the literature, polymeric nanoparticles in the 100–400 nm size range are considered optimal for passive tumor targeting in which polymeric NPs accumulate into pathological sites due to leaky vasculatures of tumors (100–1000 nm gap size) and enhanced permeability and retention (EPR) effect [19–21]. Due to their size, high surface-*to*-volume ratio, and hydrophobic core, polymeric nanobeads are widely studies in nanomedicine for *in-situ* or *ex-situ* loading for theranostic purposes. In this regard, one of the most attractive systems

are represented by optical and radionuclide imaging polymeric nanocarriers [22–24]. The use of nanoparticles provides many advantages over conventional imaging probes, such as extreme detection sensitivity and quantitative imaging [25,31].

In nuclear medicine, yttrium-90 is employed in cancer diagnosis and therapy as a pure β^- emitter with an average path of approximately 2.5 mm in human tissues [26–28] and radiolabeled PNPs were introduced as a novel class of diagnostic/therapeutic agents [29,30]. Indeed, radiolabeled NPs require a radionuclide concentration of around 10^{-10} M to obtain high detection sensitivity at high temporal and spatial resolution [31]. Optical imaging plays a critical role in biomedical sciences as it offers a convenient way to visualize and quantify various biological events directly in living systems. Among different imaging techniques, fluorescence imaging is the most widely used due to its good spatial and temporal resolution, high sensitivity and selectivity, minimal invasiveness, and excellent tunability [32]. Fluorescein isothiocyanate isomer I (FITC) dye represents a suitable fluorescent tracer to develop an "always-on" optical probe due to the high quantum yield ($\Phi = 0.93$) [33] and bright contrast. However, emission from FITC dye is often weakened by low solubility at physiological pH and poor photostability [32]. Thus, encapsulating this dye in hydrophilic NPs represents a viable alternative for making FITC useful as a fluorescent probe in nanomedicine applications.

In this framework, we studied the synthesis and characterization of acrylate-based co-polymeric nanobeads obtained *via* surfactant-free radical emulsion polymerization technique as a *proof-of-concept* for radio- and optical imaging agents nanocarriers. Methylmethacrylate (MMA) and *N,N*-dimethylacrylamide (DMAA) were chosen as co-monomers for the synthesis of p(MMA-co-DMAA) NPs due to (i) biocompatibility of MMA, and (ii) coordination ability of DMAA moieties towards rare earth trivalent ions [34]. The effects of different MMA/DMAA molar ratios, reaction times, and temperatures were studied to optimize the average hydrodynamic diameter and polydispersity index of the final colloidal nanoparticles. Spherical PNPs were confirmed by field emission scanning electron microscopy equipped with energy dispersive X-ray spectroscopy (SEM-EDS), transmission electron microscopy (TEM), and atomic force microscopy (AFM) measurements. The hydrodynamic size, colloidal stability, and swelling behavior of the nanobeads were evaluated by dynamic light scattering (DLS) and ζ-potential followed by the extensive structural characterizations *via* Fourier-transform infrared spectroscopy (FT-IR), proton and carbon nuclear magnetic resonance (^1H NMR, ^{13}C NMR), and X-ray photoelectron spectroscopy (XPS). After extensive morphostructural characterizations of pristine polymeric nanoparticles, we followed two different approaches to obtain PNPs suitable for imaging applications. First, $^{89}Y^{3+}$ ions (as a model of ^{90}Y β^- emitting radioisotope) were immobilized onto the nanocarriers surface *via* an *ex-situ* approach, using different concentrations of YCl_3 to optimize the loading percentage and loading capacity on PNPs. A comparison with the previously synthesized poly(methylmethacrylate-co-acrylic acid) NPs functionalized with diethylenetriaminepentaacetic acid chelating agent (DTPA) is reported

[12]. Herein, cytotoxicity of $^{89}Y^{3+}$-loaded nanobeads was tested *in vitro* on human glioblastoma T98G cells (as a tumor cell line model). After loading, the hydrodynamic diameter and colloidal stability of PNPs in water and RPMI-1640 culture medium were investigated at 25 °C and 37 °C up to 30 days. Then, an *in-situ* approach was used to achieve a physical encapsulation of FITC dye as the optical imaging probe inside the NPs core to form fluorescent nanocarriers. The obtained nanocarriers showed promising application in imaging and therapy for nanomedicine.

2. Materials and methods

2.1. Chemicals

All reagents and chemicals used in this work were of analytical grade or highest available purity. Methyl methacrylate (MMA, $C_5H_8O_2$, d (20 °C) = 0.936 g/mL, 100.12 g/mol), acrylic acid (AA, $C_3H_4O_2$, d (20 °C) = 1.051 g/mL, 72.06 g/mol), diethylenetriaminepentaacetic acid (DTPA, $C_{14}H_{23}N_3O_{10}$, 393.35 g/mol), *N,N*-dimethylacrylamide (DMAA, C_5H_9NO, d(20 °C) = 0.962 g/mL, 99.13 g/mol), yttrium(III) chloride hexahydrate (YCl$_3\cdot$6 H$_2$O, 303.36 g/mol), toluene (C$_6$H$_5$CH$_3$, d (20 °C) = 0.87 g/mL), methanol (CH$_3$OH, d(25 °C) = 0.791 g/mL), ethanol (CH$_3$CH$_2$OH, d(25 °C) = 0.789 g/mL), ethylene glycol (HOCH$_2$CH$_2$OH, d(25 °C) = 1.11 g/mL, and fluorescein isothiocyanate isomer I (FITC, $C_{21}H_{11}NO_5S$, 389.38 g/mol) and alizarin Red S (ARS, $C_{14}H_7NaO_7S$, 342.26 g/mol) were obtained from Sigma-Aldrich. Potassium persulfate (KPS, $K_2S_2O_8$, 270.32 g/mol) was purchased from Acros Organics. Ammonium persulfate (APS, $(NH_4)_2S_2O_8$, 228.20 g/mol) and acetone (C_3H_6O) were obtained from Merck. Milli-Q water (H$_2$O$_{up}$, resistivity 18.3 MΩ·cm) was supplied by a Zeneer Power I Scholar-UV (Human Corporation) and used for all the experiments involving the aqueous medium. All chemicals were used as received without further purification. Phosphate-buffered saline (PBS) buffer and RPMI-1640 culture medium were purchased from Sigma-Aldrich. Fetal bovine serum (FBS), L-glutamine and penicillin/streptomycin were supplied by Gibco. Trypsin-EDTA were purchased from Euroclone.

2.2. Cell line

The human glioblastoma multiforme T98G cells were purchased from European Collection of Cell Cultures. Cell lines were grown in RPMI-1640 medium supplemented with 10% fetal bovine serum (FBS), 2 mM L-glutamine, 1% penicillin/streptomycin. The cultures were maintained at 37 °C in humidified atmosphere of 95% air and 5% CO$_2$. Flasks containing asynchronous non-confluent cells were gently rinsed with 10 mL of calcium and magnesium-free D-PBS, then detached using 1 mL 1:1 v/v solution of 0.25% trypsin and 1 mM EDTA. Trypsin was neutralized using few mL of fresh culture media and then the cell solution was counted.

2.3. Polymeric nanoparticles synthesis

Poly(methylmethacrylate-co-*N,N*-dimethylacrylamide) nanoparticles (p(MMA-co-DMAA) NPs, hereafter reported as **PNPs**) were synthesized *via* surfactant-free radical emulsion polymerization technique according to previous works with modifications [12]. To optimize the average particle size and polydispersity index of PNPs the effects of reaction time (2–6 h), temperature (70–80 °C), and monomer concentrations (MMA:DMAA 10:1; 12: 1 and 14:1 molar ratios) were investigated, and the complete conditions for the as-synthesized **PNPs-1** to **-6** are reported in Table S1 in the Supporting Information and selected p (MMA-co-DMAA) samples are reported below. The polymerization reactions were carried out in a 250 mL two round-bottom flask equipped with a water-cooled reflux condenser and filled with 20 mL of Milli-Q water. 1 mL (9.35·10^{-3} mol) of MMA monomer was added and different concentrations of DMAA were used (in molar ratios ranging

from 10:1–14:1). At this stage, 10 mL of toluene was added, and the flask was immersed in an oil bath at the selected temperature. The reaction mixture was degassed with Ar$_{(g)}$ flow for 15 min. Upon reaching the desired temperature, the polymerization was initiated by injection of 5 mL of aqueous solution of the radical initiator (50 mg KPS, 80 °C or 50 mg APS, 70 °C). Reactions were carried out at three-time intervals, *i.e.,* 2, 4, and 6 h under constant magnetic stirring (approximately 1500 rpm). After cooling to room temperature, the as-synthetized colloidal suspensions were washed with ultrapure water (7 × 5 mL) in centrifuge at 5000 rpm for 20 min. After the synthesis, the products were freeze-dried to obtain solid pellet for further use. The main characterizations of selected p(MMA-co-DMAA) NPs are herein reported, together with dispersity, Đ = M$_w$/ M$_n$ [35] obtained by GPC analysis.

Main characterizations of selected p(MMA-co-DMAA) NPs:

PNPs-4a: (MMA:DMAA 10:1 molar ratio, 2 h, KPS, 80 °C) Yield 25% wt/wt. M$_n$ = 3060 Da, M$_w$ = 3610 Da and Đ = 1.18.

^{1}H NMR (400 MHz, CDCl$_3$, ppm): δ 3.60 (—OCH$_3$, 3 H), 2.99 + 2.89 (—N(CH$_3$)$_2$, 6 H), 2.49 (—CH—, 1 H), 1.81 (—CH$_2$— inner, 2 H), 1.59 (—CH$_2$— outer, 2 H), 1.25 (—CH$_3$, 3 H). MMA/DMAA integral ratio 9:1.

PNPs-4b: (MMA:DMAA 10:1 molar ratio, 4 h, KPS, 80 °C) Yield 20% wt/wt. M$_n$ = 2260 Da, M$_w$ = 4400 Da and Đ = 1.94.

^{1}H NMR (300 MHz, CDCl$_3$, ppm): δ 3.58 (—OCH$_3$, 3 H), 2.97 + 2.88 (—N(CH$_3$)$_2$, 6 H), 2.34 (—CH—, 1 H), 1.80 (—CH$_2$— inner, 2 H), 1.55 (—CH$_2$— outer, 2 H), 1.24 (—CH$_3$, 3 H). MMA/DMAA integral ratio 10:1.

^{13}C NMR (300 MHz, CDCl$_3$, ppm): δ 178.25 (—C═O ester, 1 C), 177.99 (—C═O amide, 1 C), 54.48 (—CH$_2$— inner, 1 C), 51.96 (—OCH$_3$, 1 C), 44.97 (quaternary C, 1 C), 44.61 (—N(CH$_3$)$_2$, 2 C).

PNPs-5a: (MMA:DMAA 12:1 molar ratio, 2 h, KPS, 80 °C) Yield 1% wt/wt. M$_n$ = 2580 Da, M$_w$ = 2790 Da and Đ = 1.08.

^{1}H NMR (300 MHz, CDCl$_3$, ppm): δ 3.60 (—OCH$_3$, 3 H), 2.99 + 2.89 (—N(CH$_3$)$_2$, 6 H), 1.81 (—CH$_2$— inner, 2 H), 1.43 (—CH$_2$— outer, 2 H), 1.26 (—CH$_3$, 3 H). MMA/DMAA integral ratio 4:1.

PNPs-5b: (MMA:DMAA 12:1 molar ratio, 4 h, KPS, 80 °C) Yield 9% wt/wt. Mn = 2230 Da, Mw = 3640 Da and Đ = 1.63.

^{1}H NMR (300 MHz, CDCl$_3$, ppm): δ 3.59 (—OCH$_3$, 3 H), 2.98 + 2.89 (—N(CH$_3$)$_2$, 6 H), 2.35 (—CH—, 1 H), 1.80 (—CH$_2$— inner, 2 H), 1.56 (—CH$_2$— outer, 2 H), 1.24 (—CH$_3$, 3 H). MMA/DMAA integral ratio 12:1.

^{13}C NMR (300 MHz, CDCl$_3$, ppm): δ 178.08 (—C═O ester, 1 C), 177.75 (—C═O amide, 1 C), 54.29 (—CH$_2$— inner, 1 C), 51.76 (—OCH$_3$, 1 C), 44.79 (quaternary C, 1 C), 44.43 (—N(CH$_3$)$_2$, 2 C), 29.62 (—CH-, 1 C).

PNPs-6a: (MMA:DMAA 14:1 molar ratio, 2 h, KPS, 80 °C) Yield 4% wt/wt. M$_n$ = 1950 Da, M$_w$ = 3120 Da and Đ = 1.60.

^{1}H NMR (300 MHz, CDCl$_3$, ppm): δ 3.60 (—OCH$_3$, 3 H), 3.00 + 2.89 (—N(CH$_3$)$_2$, 6 H), 2.32 (—CH—, 1 H), 1.81 (—CH$_2$— inner, 2 H), 1.56 (—CH$_2$— outer, 2 H), 1.26 (—CH$_3$, 3 H). MMA/DMAA integral ratio 10:1.

PNPs-6b: (MMA:DMAA 14:1 molar ratio, 4 h, KPS, 80 °C) Yield 8% wt/wt. M$_n$ = 2370 Da, M$_w$ = 3600 Da and Đ = 1.52.

^{1}H NMR (300 MHz, CDCl$_3$, ppm): δ 3.59 (—OCH$_3$, 3 H), 2.98 + 2.89 (—N(CH$_3$)$_2$, 6 H), 2.49 (—CH—, 1 H), 1.81 (—CH$_2$— inner, 2 H), 1.25 (—CH$_3$, 3 H). MMA/DMAA integral ratio 12:1.

^{13}C NMR (300 MHz, CDCl$_3$, ppm): δ 178.22 (—C═O ester, 1 C), 178.00 (—C═O amide, 1 C), 54.56 (—CH$_2$— inner, 1 C), 51.95 (—OCH$_3$, 1 C), 45.03 (quaternary C, 1 C), 44.69 (—N(CH$_3$)$_2$, 2 C).

The synthetic procedure, structure, and main characterizations of p (MMA-co-AA)-DTPA nanoparticles (hereafter reported as **PNPs-DTPA**) are reported in the Supporting Information.

2.4. Labeling of PNPs with yttrium ions (Y^{3+})

p(MMA-co-DMAA) and p(MMA-co-AA)-DTPA NPs were directly labeled with $^{89}Y^{3+}$ ions by adding 2 mL of a YCl$_3\cdot$6 H$_2$O aqueous solution to the solid nanoparticles (final pH 4.5). Different NPs/YCl$_3$ weight

ratios, *i.e.*, 5/1, 10/1, 20/1, and concentrations of YCl_3 (0.2–1.2 mg/mL) were tested to optimize the loading percentage and loading capacity. Triplicate samples of Y-labeled NPs (2 mL each) were allowed to react at 25 °C for 1 h in the dark. Y-labeled nanoparticles were separated from unbound YCl_3 by centrifugation (14,000 rpm, 20 min, +8 °C) and the product was freeze-dried to obtain solid pellet for further use. To determine the loading percentage (%L) and the loading capacity (%LC) of yttrium ions on the nanoparticles surface, 1 mL of the supernatant, obtained after centrifugation, was transferred into a 10 mL-calibrated flask. To this solution, 1 mL of alizarine red S (ARS, 3.33 mM) aqueous solution (at pH 4.5) was added and mixed [36]. The absorbance of the resulting-colored solution was measured immediately at 520 nm (in light-protected conditions) and the concentration of $Y^{3+}_{(aq)}$ was then determined according to ARS calibration curve, reported in Fig. S1 together with the UV-Vis absorption spectrum. %L and %LC were calculated using the following equations [37]:

$$\%Loading = \%\boldsymbol{L} = \frac{mol \ \ Y^{3+}_{initial} - mol \ \ Y^{3+}_{supernatant}}{mol \ \ Y^{3+}_{initial}} \bullet 100$$

$$\%Loading \ \ capacity = \%\boldsymbol{LC} = \frac{Amount \ \ of \ \ Y^{3+}_{on} \ \ _{PNPs}}{weight \ \ of \ \ NPs} \bullet 100$$

where *mol* $Y^{3+}_{initial}$ initial is the number of moles of $YCl_{3(aq)}$ stock solution added to NPs for the loading; *mol* $Y^{3+}_{supernatant}$ is the number of moles of $YCl_{3(aq)}$ found in the supernatant after the first centrifuge and obtained by calibration curve interpolation. *Amount of* Y^{3+}_{on} *PNPs* is the quantity expressed as grams of Y^{3+} immobilized on nanobeads surface. These measurements were done in triplicate and are presented as mean ± standard deviation.

2.5. Release studies of yttrium ions (Y^{3+})

To study the release of yttrium ions from nanobeads surface, Y^{3+}-loaded nanoparticles were dispersed in H_2O_{up} at pH = 7.0 and concentration = 0.24 mg/mL. The suspension was maintained under gentle mixing at $(37 \pm 1)°C$ throughout the experiment. At definite time intervals from 0 to 30 days, a 1 mL aliquot was withdrawn, and the supernatant was analyzed spectrophotometrically at 520 nm after the addition of ARS solution (dilution 1:10 v/v) by interpolation of the standard calibration curve.

2.6. Preparation of dye-loaded polymeric NPs

Two different co-polymeric nanobeads were loaded with FITC isomer I dye to obtain dye encapsulated p(MMA-co-DMAA)/FITC (hereafter reported as **PNPs-F**) and p(MMA-co-AA)-DTPA/FITC (hereafter reported as **PNPs-DTPA-F**) nanoparticles synthesized in MMA:DMAA 10:1 molar ratio and MMA:AA 12:1 molar ratio, respectively. 0.0100 g of FITC isomer I dye were first dissolved in 3 mL of acetone at a concentration of 3.3 mg/mL. This FITC solution was then added to the mixture of the two monomers in water/toluene 2:1 v/v. Then, the synthesis of polymeric NPs was accomplished following the procedure described for the preparation of unloaded PNPs at 80 °C for 2 h using KPS as the radical initiator (see paragraph 2.3). The FITC molecules that were not encapsulated in the nanoparticles were discarded after centrifugation at 5000 rpm for 20 min (7 × 5 mL H_2O_{up}), and the yellow product was collected and stored at room temperature in the dark for further use.

2.7. Clonogenic survival assay

To study the cytotoxic effect of the NPs on T98G cells, the clonogenic assay developed by Puck and Marcus was used [38]. The clonogenic assay allows assessment of decreased or increased survival over time. After plating at a very low density, cells are allowed to grow until colonies are observed. It is assumed that each colony originates from a single cell. Before the assay, polymeric NPs were sterilized under UV-C lamp at room temperature for 24 h. The polymeric NPs were reconstituted in RPMI-1640 complete medium at three different concentrations: 10 µg/mL, 30 µg/mL, and 50 µg/mL. Briefly, T98G cells in the exponential growth phase were seeded at concentrations of $2 \cdot 10^4$ cells/cm^2 into 25 cm^2 flasks and incubated for 24 h in 5% CO_2 humidified incubator at 37 °C with unlabeled and Y^{3+}-labeled polymeric nanoparticles. For each experiment, a control group was prepared. Following 24-hour exposure, the cells were rinsed several times with PBS buffer, detached from the flasks and counted. Then, 5 cm Petri dishes were seeded with 400 cells and cell cultures incubated for 10–14 days at 37 °C in 5% CO_2 in air and 95% humidity before staining with 1% w/v crystal violet. Colonies exceeding 50 cells were scored manually and represent surviving cells. The average colony count for the five dishes was used to calculate plating efficiency (PE) defined as number of colonies counted/number of cells plated [39]. Plating efficiencies were determined for each treatment condition and normalized to an untreated control to provide the Surviving Fraction (S.F.). The surviving fraction was calculated based on following equation [40]:

$$Surviving \ \ fraction = S.F. = \frac{mean \ \ colony \ \ counts}{cell \ \ plated \bullet plating \ \ efficiency}$$

All experiments were performed from three to five times and the results were expressed as mean of S.F. ± standard error of the mean (S.E.M.).

2.8. Colloidal stability of polymeric nanoparticles

To investigate the colloidal stability of the prepared NPs, 0.1 mg of their solid pellet was added to 1 mL of H_2O_{up} or RMPI-1640 complete culture medium to obtain a nano-formulation at concentration 0.1 mg/mL. At prescriptive intervals (0, 2, 4, 6, 8, 12, 24 h up to 30 days), changing in the particle size was monitored by DLS in RPMI-1640 complete medium, at 37 °C. Data were processed and reported as mean ± standard deviation over three measurements. Colloidal stability was also investigated with SAXS measurements, within 24 h.

2.9. Swelling measurements

A 3 mg of dried polymeric nanoparticles were dispersed in 1 mL of the desired medium, obtaining a 3 mg/mL colloidal suspension. The colloids were maintained under stirring for 1 h to completely swell. Swelling behavior was investigated in different solvents: methanol, ethanol, ethylene glycol, and in various acidic and basic pHs in the range of 3–11. Solution at different pHs were prepared by addition of HCl (1.0 M) and NaOH (1.0 M) to ultrapure water. The solution pH was measured by a pH-meter (accuracy ± 0.01). Swelling was evaluated in terms of mean hydrodynamic diameter and size distribution.

2.10. Biological sample preparation for TEM observations

PNPs internalized into T98G cells were prepared by a well-established analytical protocol to be observed by TEM [41], and briefly reported in the Supporting Information.

3. Characterization techniques

To characterize the surface chemistry of the polymeric nanoparticles, Fourier transform infrared spectroscopy (FT-IR) measurements were conducted with Bruker Vertex 70 instrument. The samples deposited on Thallium Bromoiodide (KRS-5) plate were scanned from 4000 to 400 cm^{-1}. ATR-mode spectra were recorded in the 4000–600 cm^{-1} range. Resolution of 4 cm^{-1} with a minimum of 32 scans was selected for these measurements.

Molecular weight properties of the polymeric nanoparticles systems were determined by gel permeation chromatography (GPC). GPC

analyses at room temperature were performed on a Perkin Elmer instrument equipped with LC90J spectrophotometric UV detector set at 270 nm and 10 μm polystyrene-divinylbenzene column. Chloroform (HPLC grade) was used as eluent, pumped at a flow rate of 1.0 mL/min by a Varian 9001 LC pump. Monodisperse polystyrene standards were used for calibration. Number-average molecular weight (M_n), weight-average molecular weight (M_w), and molecular weight dispersity ($Ð = M_w/ M_n$) were determined for each colloidal system [35].

The hydrodynamic diameters ($<2R_H>$), ζ-potentials, and polydispersity indexes (PDI) of polymeric nanoparticles were measured by dynamic light scattering (DLS) on a Malvern Zetasizer Nano ZS90 instrument at 25 °C using a 4 mW laser light with the wavelength of 632.8 nm and an automatic attenuator. Measurements were done in triplicate and reported as mean ± standard deviation.

^{1}H NMR and ^{13}C NMR spectra were recorded on a Bruker Avance III 400.13 MHz spectrometer in CDCl$_3$ (^{1}H NMR CDCl$_3$: 7.26 ppm, ^{13}C NMR CDCl$_3$: 77.16 ppm) and the chemical shift values were given in parts per million (δ, ppm).

UV-Vis spectra were recorded using a spectrophotometer Varian Cary 100 (wavelength range of 200–800 nm) at room temperature. The quartz cells having 1 cm optical path length were used.

SAXS measurements were performed at SAXSLab Sapienza with a Xenocs Xeuss 2.0 Q-Xoom system, equipped with a micro-focus Genix 3D X-ray Cu source (λ = 0.1542 nm), a two-dimensional Pilatus3 R 300 K detector placed at variable distance from the sample. The samples were loaded in disposable glass capillaries sealed with hot-glue and placed in a thermalized capillary holder (25 or 37 °C) in the sample chamber at reduced pressure (~0.2 mbar). Details on data acquisition and treatment are reported in the Supporting Information.

Atomic Force Microscopy (AFM) images were recorded on Veeco Instrument, Multimode™ model equipped with a Nanoscope IIIa controller, using a Bruker RTESP-300 probe in tapping-mode. The samples were prepared by drop casting onto a Si/SiO$_2$ substrate from their aqueous dispersion.

The morphology of the PNPs was assessed by an Auriga Zeiss field emission scanning electron microscopy supported by energy dispersive X-ray spectroscopy detector (FESEM-EDS) instrument. The samples were drop casted on conducting silicon substrate from their aqueous solution. The surface morphology was further studied using a variable pressure scanning electron microscope (VP-SEM-2EDS, Hitachi SU-3500) supported by dual-energy dispersive X-ray spectroscopy detectors (dEDS) arranged in parallel configuration (Bruker, XFlash® 6|60) able to perform high sensitivity elemental analysis by their large active area of 60 mm^2 each. The hydrated particles in their native state were observed without using conductive coating. VP-SEM combined with Peltier cool stage control allowed imaging of hydrated cells under varying pressure conditions as well as limiting water vapour loss through the control of stage temperature [42,43].

TEM images were acquired with a Zeiss EM10 electron microscope operating at 60 kV. Samples were placed onto a 300-mesh copper grid coated with holey carbon film and then air-dried [44].

X-ray photoelectron spectroscopy (XPS) analyses were carried out with a homemade instrument, consisting of preparation and analysis UHV chambers separated by a gate valve. The used X-ray radiation is a non-monochromatized Mg Kα (1253.6 eV). The analysis chamber is equipped with a six-degree-of freedom manipulator and a 150 mm mean radius hemispherical electron analyzer with a five-lens output system combined with a 16-channel detector giving a total instrument resolution of 1.0 eV. Samples were introduced in the preparation chamber and left outgassing overnight at a base pressure of about 10^{-8} Torr, before introduction in the analysis chamber. Typical vacuum pressure in the analysis chamber during measurements was in the 10^{-8}-10^{-9} Torr range. Spectra were acquired at C1s, N1s, O1s, Cl2p, S2p, and Y3d core level. Details on data acquisition and treatment are reported in the Supporting Information.

Fluorescence microscopy images were recorded with a fluorescence

microscopy for live imaging Apotome, Carl Zeiss. Samples were deposited by drop casting from their aqueous solution on a glass slide and observed with 63× oil immersion objective.

4. Results and discussion

4.1. Synthesis of PNPs

Surfactant-free radical emulsion polymerization is a well-established method to synthetize acrylates-based polymeric spherical nanoparticles [12]. Two vinyl monomers, *i.e.*, methyl methacrylate and *N,N*-dimethylacrylamide, were polymerized under mild conditions (70 °C or 80 °C) using KPS or APS as the radical initiator. The nanostructured p(MMA-co-DMAA) polymers were obtained as shown in Scheme 1 and isolated after purification steps in centrifuge to remove unreacted monomer and non-nanostructured by-products. This step critically affects the overall yields but assure low size distribution and in turn high quality of the NPs.

To evaluate the effect of different MMA/DMAA molar ratios and polymerization temperatures, the obtained PNPs were characterized in terms of size distribution, morphology, and ζ-potential. The hydrodynamic diameter (reported as intensity distribution) of p(MMA-co-DMAA) NPs obtained with three different MMA/DMAA molar ratios are compared in Fig. 1, and the experimental values are reported in Table S2 in the Supporting Information. The average $< 2R_H>$ and PDI showed a dependence with MMA/DMAA molar ratio, reaction time, and temperature. The plot reported in Fig. 1(a) shows the hydrodynamic size distribution of p(MMA-co-DMAA) NPs obtained at 70 °C. For the MMA/DMAA 10/1 molar ratio, increasing the reaction time from 2 h to 6 h led to a significant increase in the size (hydrodynamic size > 700 nm) and polydispersity index (> 0.500) of the obtained nanoparticles (gray bars in Fig. 1(a). The increasing of MMA content in the MMA/DMAA reaction mixture (from 10:1–12:1 molar ratio) caused an increase in the particle size distribution leading to polydisperse samples (not shown here). Besides, with the 14:1 molar ratio (magenta bars in Fig. 1(a)), an average size of 395 ± 190 nm and 340 ± 140 nm were obtained for a reaction time of 2 h and 4 h, respectively; however, polydisperse samples with size higher than 300 nm are obtained in all cases at 70 °C.

Fig. 1(b) shows the average particles size of the polymeric NPs synthesized at 80 °C. In all cases (MMA/DMAA 10:1, 12:1, 14:1 molar ratios), similar trends were observed. Indeed, an increase in the hydrodynamic diameter occurred for a reaction time of 4 h with $< 2R_H>$ values in the 220–615 nm range, although no significant changes in the PDI values were observed (except for MMA:DMAA 12:1 molar ratio, reaction time 2 h sample, see Table S2 in the Supporting Information).

The surface charge of p(MMA-co-DMAA) NPs in water (reported as ζ-potential values in Table S2 in the Supporting Information), was investigated at 25 °C. All tested polymeric nanobeads exhibited a negative value (Fig. 1(b)) suggesting: (i) a good colloidal stability, since colloidal samples with ζ-potential ≤ –30 mV possess long-term stability against aggregation; (ii) electrostatic attraction could be the main driving force for adsorbing Y^{3+} ions onto the outer PNPs surface for next studies. At 70 °C, the yield of the reaction (calculated as weight of nanostructured fraction obtained from the crude product with respect to the weight of the used monomers) was < 6%. Promising syntheses conducted at 80 °C (**PNPs-4, PNPs-5,** and **PNPs-6**) provided stable and less polydisperse nanobeads with yield ≥ 20% wt/wt. According to literature, for nanostructured polymers synthesized with emulsion polymerization, an increase in the yield of the reaction, *i.e.*, monomers conversion, up to 70%, can be achieved by increasing the reaction time [45]. However, as demonstrated, prolonged reaction time negatively affects the NPs size distribution with an increase in the PNPs hydrodynamic diameter above 500 nm.

Particularly attracting was **PNPs-4a** sample (MMA:DMAA 10:1 molar ratio, reaction time 2 h) that showed a $< 2R_H> = 220 ± 90$ nm
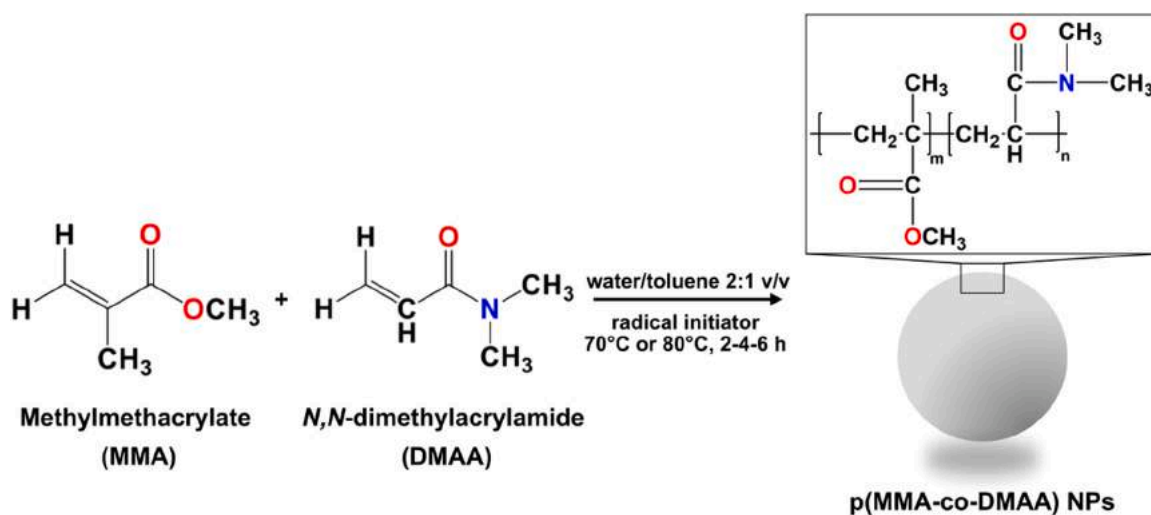
Scheme 1. Synthesis strategy for the preparation of p(MMA-co-DMAA) polymeric nanobeads.
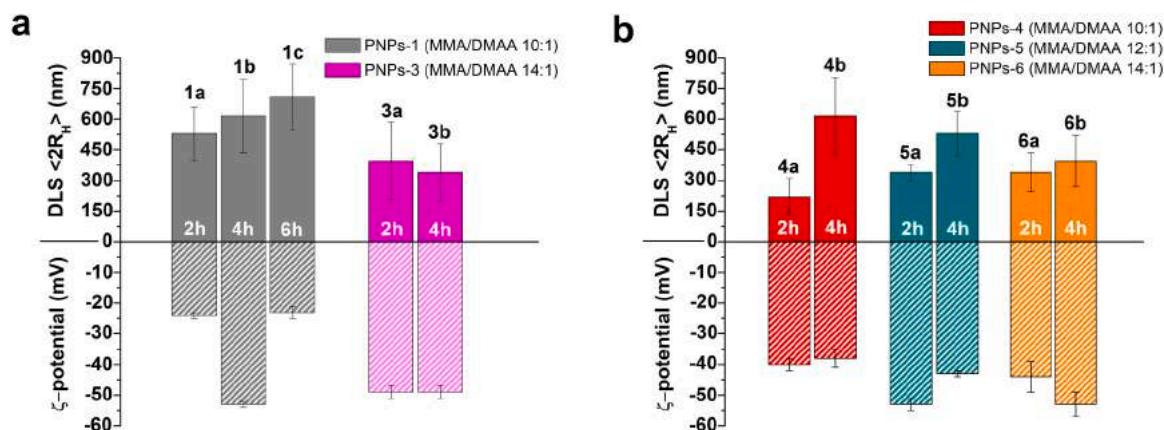

Fig. 1. DLS average hydrodynamic diameter ($\pm$ standard deviation) (plain bars) and ζ-potential values (bars with pattern): (**a**) p(MMA-co-DMAA) NPs (PNPs-1 and PNPs-2) obtained at 70 °C (**b**) p(MMA-co-DMAA) NPs (PNPs-4, PNPs-5 and PNPs-6) obtained at 80 °C. Data with polydisperse size distribution are not shown. The relative values of DLS mean size and ζ-potential are listed in Table S2 in the Supporting Information.

(PDI = 0.117), ζ-potential = -40 ± 2 mV with yield of 25.0% wt/wt.

4.2. Morphological characterization of pristine PNPs

The morphology of nanobeads is another critical hallmark for exploiting surface properties. Thus, FESEM was used to determine their morphology and size, as dried samples. A direct comparison of the shapes and sizes of **PNPs-4a** (MMA:DMAA 10:1, reaction time 2 h) with **PNPs-5b** (MMA:DMAA 12:1, reaction time 4 h), and **PNPs-6b** (MMA: DMAA 14:1, reaction time 4 h) as representative samples can be found in Fig. 2. As shown in Fig. 2(a,b), **PNPs-4a** (MMA:DMAA 10:1) displayed at solid state a spherical shape with irregular surface and quite uniform size distribution (d = 237 ± 48 nm), similarly **PNPs-5b** (MMA:DMAA 12:1, diameter of 331 ± 44 nm) were all spherical-shaped, but with featureless smooth surface. In both cases, the particle size measured with FESEM is in good agreement with that determined by the dynamic light scattering. For **PNPs-6b** (MMA:DMAA 14:1, Fig. 2(c)), large network of self-aggregated nanoparticles with porous surface was found, the mean diameter of near spherical-shaped NPs was 236 ± 41 nm. Considering the solid-state diameter, it is possible to estimate the mean surface area (SA) and the surface-*to*-volume ratio (S/V) for a spherical nanoparticle [46]. Results are as follows. **PNPs-4a:** SA = 0.176 μm^2, S/V = 0.025 nm^{-1}; **PNPs-5b:** SA = 0.344 μm^2, S/V = 0.018 nm^{-1}; **PNPs-6b:** SA = 0.175 μm^2, S/V = 0.025 nm^{-1}.

By contrast, for polymeric nanoparticles synthesized at 70 °C, *i.e.*, **PNPs-1** to **PNPs-3** samples, FESEM analyses showed polydisperse samples with irregular shape and rough surface topology (Fig. S2 in the Supporting Information). More accurate indication about the morphology of the PNPs synthesized at 80 °C were obtained from tapping mode AFM observations on nanobeads suspension deposited on a glass slide by drop casting (Fig. 2(d-f)). The two-dimensional AFM images of **PNPs-4a** (Fig. 2(d)) and **PNPs-5b** (Fig. 2(e)) showed spherical-shaped nanoparticles with diameter in accordance with FESEM images. On the other hand, by the optimization of the reaction conditions it is possible to modulate the surface morphology [15]. Indeed, for **PNPs-6b** AFM (Fig. 2(f)), operating at 25 °C and ambient pressure, showed no evidence of pore formation. Further evidence of smooth, non-porous nanoparticles surface morphology arises from three-dimensional AFM profiles reported in Fig. S3. As it is possible to note, when investigated *via* FESEM (Fig. 2(c)) **PNPs-6b** reveal an irregular appearance, with holes and elongated structures, in contrast with the well-defined spherical morphology shown when analyzed *via* AFM (Fig. 2(f)). This is probably an artifact due to the ultra-high vacuum conditions necessary to perform FESEM analysis, which can cause implosion of the particles with subsequent loss of their structure. On the other hand, AFM being performed in air in tapping mode, is a milder technique which keeps the soft particles unaltered. For completeness, comparison between FESEM and AFM size analysis statistics is reported
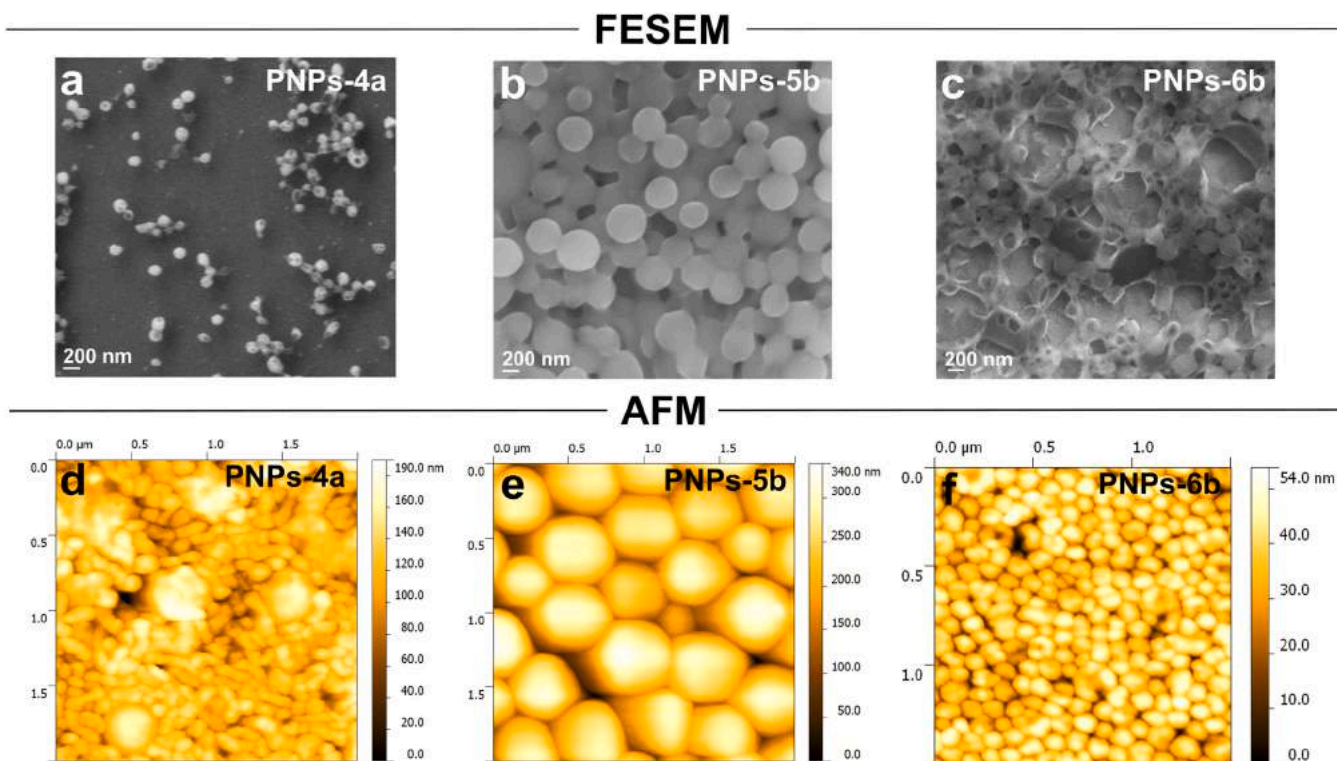
FESEM

AFM

Fig. 2. High resolution FESEM images of (**a**) PNPs-4a; (**b**) PNPs-5b and (**c**) PNPs-6b deposited by drop casting on silicon stub. AFM images of (**d**) PNPs-4a; (**e**) PNPs-5b and (**f**) PNPs-6b deposited by drop casting on Si/SiO$_2$ stub.
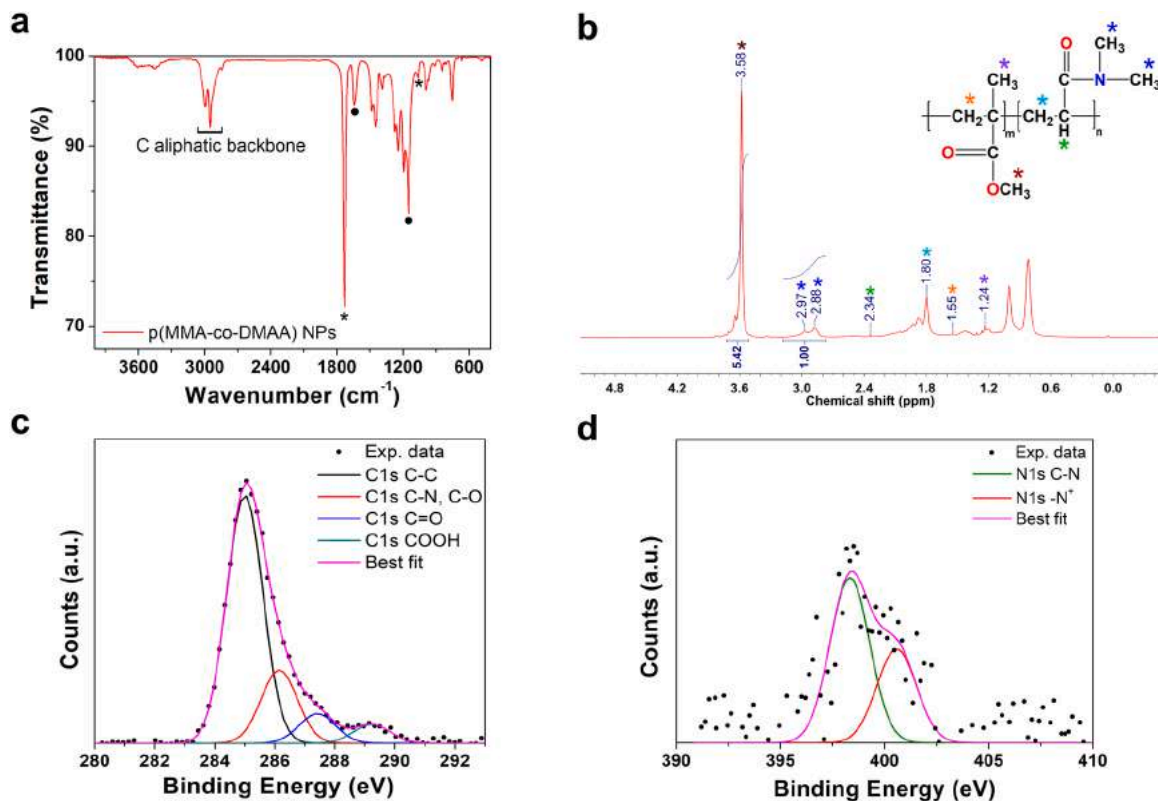

Fig. 3. p(MMA-co-DMAA) NPs (PNPs-4a, MMA:DMAA 10:1, reaction time 2 h) characterizations: (**a**) FT-IR spectrum (film from CHCl$_3$). Main stretching vibrations of MMA comonomer (asterisk) and DMAA comonomer (black dot) inside the PNPs structure are evidenced. (**b**) Representative ^{1}H NMR spectrum of p(MMA-co-DMAA) obtained with MMA/DMAA 10/1 molar ratio (reaction time 4 h, T = 80 °C). XPS spectra (sample deposited on TiO$_2$ stub from their aqueous solution at (**c**) C1s and (**d**) N1s core level.

in Fig. S4.

4.3. Structural characterization of pristine PNPs

The chemical structure of p(MMA-co-DMAA) NPs synthesized at 80 °C was characterized by FT-IR, XPS spectroscopy, ^{13}C and ^{1}H NMR and results on sample **PNPs-4a** (MMA:DMAA 10:1, reaction time 2 h) is herein discussed as representative of this class of nanobeads. Based on the FT-IR spectrum (Fig. 3a), all the peaks originating from NPs after polymerization reaction including $-C{=}O$ groups ($\nu = 1730$ cm^{-1}), $-CH_2$ of the polymer backbone ($\nu_s = 2850$ cm^{-1}, $\nu_{as} = 2935$ cm^{-1}, $\delta_s = 1480$ cm^{-1}) and $-CH_3$ ($\nu_{as} = 2984$ cm^{-1}, $\delta_s = 1380$ cm^{-1} and $\delta_{as} = 1450$ cm^{-1}), as well as $-C{=}O$ stretching vibration of tertiary amide ($-CON(CH_3)_2$) at 1635 cm^{-1} and of $-C$-N at 1132 cm^{-1} are evident in the p(MMA-co-DMAA) spectrum, although there are no evident peaks of the $(CH_3)_2N-$ group due to the overlap with aliphatic $-CH_2/-CH_3$ groups in the 2810–2825 cm^{-1} region. Moreover, the band observed at 1070 cm^{-1}, assigned to the stretching vibration of C–O–C group of MMA comonomer (Fig. 3(a)). The FTIR spectra of the pristine MMA and DMAA (Fig. S5 in the Supporting Information) exhibited a more intense absorption bands associated with the stretching of C=C (vinyl) and =CH sp^2 (vinyl) at 1610–1620 cm^{-1} and 3100 cm^{-1}, respectively. Both these bands are absent in the nanostructured copolymer structure, confirming the successful copolymerization of the monomers.

XPS analyses provided further surface information about the chemical composition of the PNPs deposited on TiO$_2$ stubs. For the pristine samples of p(MMA-co-DMAA) NPs, spectra were collected at C1s, N1s and O1s core level (all BE (eV), FWHM (eV), relative intensity values and proposed signals assignments are reported in Table S3 in the Supporting Information). C1s spectra (Fig. 3(c)) has four components at 285.00, 286.5, 288.0 and 289.5 eV BE associated with C-C, C-N and C-O, C=O and COOH carbons, respectively. N1s spectra (Fig. 3(d)) showed two components: the first centered at about 399.0 eV, as expected for amine-like nitrogen, and the second one at about 401.0 eV due to protonated nitrogen. O1s spectrum (Fig. S6 in the Supporting Information) also showed four different oxygen atoms belonging to TiO$_2$ stub (*ca.* 529.5 eV BE), C=O functional groups (532.0 eV BE), hydroxyl moieties (–OH, 533.0 eV BE) and physisorbed water (small contribution at about 534.5 eV BE). Both ATR-FTIR and the mentioned XPS results confirm the molecular structure of the polymeric nanobeads (shown in Scheme 1).

Quantitative information about nanoparticle composition and monomers conversion can be obtained through ^1H NMR and ^{13}C NMR. For all the p(MMA-co-DMAA) NPs samples, two typical signals in the 2.90–3.00 ppm range and at about 3.60 ppm resulted from the nonequivalent –CH$_3$ protons of the tertiary amide of DMAA and –CH$_3$ protons of the –OCH$_3$ group of MMA comonomer, respectively. This suggested the successful copolymerization between DMAA and MMA. Based on the intensities of the –N(CH$_3$)$_2$ and –OCH$_3$ analyzed in the ^1H NMR spectra, the molar ratio of MMA to DMAA in the as-prepared PNPs can be calculated. Theoretical and experimental molar ratios are reported in Table S4 in the Supporting Information. For simplicity, only ^1H NMR spectrum of **PNPs-4b** (MMA:DMAA 10:1, reaction time 2 h), is reported in Fig. 3(b) (all ^1H- and ^{13}C NMR spectra are reported in Fig. S7-S8 in the Supporting Information). The best MMA/DMAA conversion were achieved for **PNPs-4b** (MMA:DMAA 10:1, reaction time 4 h) and **PNPs-5b** (MMA:DMAA 12:1, reaction time 4 h) samples in which the integration of the unique resonances of comonomers, *i.e.*, proton signals of –OCH$_3$ and –N(CH$_3$)$_2$ groups, gave an experimental MMA:DMAA molar ratio equal to 10:1 and 12:1, according to the theoretical one. Besides, for polymerization reactions conducted at 70 °C, the monomer conversion rate was *ca.* 50%. Lower experimental monomers ratios compared to the theoretical one is due to the reaction conditions, which did not allow for a full conversion of the monomers into copolymeric chains. In all NMR spectra, signals at 1.59 and 1.81 ppm of –CH$_2$– on polymer chain, and 1.5 ppm of –CH$_3$ of MMA unit were found, whereas no signals associated with free monomers, (*i.e.*,

vinyl proton signals in the 5.5–6–5 ppm range), were observed in all the spectra confirming the effectiveness of the purification steps in centrifuge. M_n, M_w and Đ were estimated *via* gel permeation chromatography (GPC), calibrated with polystyrene standards in CHCl$_3$. As expected for radical emulsion polymerization, molecular weights of p(MMA-co-DMAA) NPs increased with reaction time ranging from 2500 to 4500 Da. All the molecular weights were calculated by interpolation of the standard calibration curve. All the GPC parameters are listed in the experimental section.

According to the characterization results, it can be assessed that PNPs synthesized at 70 °C showed poor morphology, low reaction yield, and low monomers conversion, thus they will not be considered for further studies. **PNPs-4**, **PNPs-5** and **PNPs-6** synthesized at 80 °C were selected for the investigations in the following paragraphs.

4.4. Loading of yttrium ions on PNPs

As a *proof-of-concept*, the as-prepared PNPs were tested as carriers to deliver Y^{3+} ions. To do so, yttrium ions were immobilized on the nanobeads surface *via* chelating groups and a comparison with previously synthetized p(MMA-co-AA)-DTPA NPs (**PNPs-DTPA, with** MMA: AA:DTPA 12:1:0.025 molar ratio) was reported [12]. As it is known, diethylenetriaminepentaacetic acid (DTPA) is an acyclic cationic metal chelating agent able to form a thermodynamically stable complex with Y^{3+} ions with log K of 22.5 [47]. However, DTPA showed a limited solubility in water (< 0.5 g/100 mL at 20 °C, pK$_a$ 1.80), thus affecting the stealth properties of hydrophilic PNPs and the interactions with the surrounding environment. Since DTPA has a high affinity for metals, the presence of competing cations, *e.g.*, Ca^{2+}, Mg^{2+}, Fe^{2+}/Fe^{3+}, Mn^{2+}/Mn^{4+}, causes a dissociation of the metal with less half-life of the metal-chelator complex. As a comparison, p(MMA-co-DMAA) NPs can form coordination complexes with trivalent ions [34], thus these systems were tested for Y^{3+} chelation on the surface of nanobeads without the addition of DTPA or any other chelating agent [48]. Complete data of loading percentage and loading capacity of Y^{3+} (calculated with ARS chelating agent, using the calibration curve in Fig. S1 in the Supporting Information) are reported in Table S5 in the Supporting Information. The Y^{3+} loading was optimized at (92 ± 1)% for p(MMA-co-DMAA) NPs (**PNPs-6b**), comparable with p(MMA-co-AA)-DTPA-Y NPs results, with Y^{3+} loading in the 44–93% range. For p(MMA-co-DMAA)-Y NPs, increase in the yttrium ions loading was achieved with a YCl$_3$ loading solution of 1.2 mg/mL and a PNPs/YCl$_3$ 10/1 molar ratio, *i.e.*, **PNPs-5a**, **PNPs-6b**, although a decrease in the %L was obtained in the presence of different amounts of nanobeads, *i.e.*, PNPs/YCl$_3$ 5/1 and PNPs/YCl$_3$ 20/1 molar ratios, for which the loading percentage was (12 ± 1)% and (32 ± 4)%, respectively. A representation of the loading behavior of the two nanobeads type for PNPs/YCl$_3$ weight ratio is shown in Fig. 4(a). The comparison between **PNPs-DTPA** and p(MMA-co-DMAA) NP$_S$ demonstrated that there are only slight differences in the loading percentage of Y^{3+}. Indeed, a loading %L *ca.* 90% and loading capacity %LC *ca.* 50% were obtained for both p(MMA-co-DMAA) NPs (*e.g.*, sample **PNPs-5b**) and p(MMA-co-AA)-DTPA in the optimized conditions. As reported in literature, p(*N,N*-dimethylacrylamide) homo- and copolymers do not show retention capacity towards bivalent and trivalent ions (*e.g.*, Cu^{2+}, Cd^{2+}, Co^{2+}, Ni^{2+}, Pb^{2+}, Zn^{2+}) thus demonstrating advantage in nanomedicine over conventional chelating agents in the presence of different metal cations [49]. Moreover, DMAA polymers revealed to have good antibacterial and antiviral properties and non-fouling properties due to the steric hindrance effect of the amide group [50]. The adsorption of other species, *i.e.*, molecules, ions, on the surface of PNPs can significantly impact the electrical surface characteristics, thus affecting the colloidal stability of the formulations. To evaluate the stability in aqueous medium after the loading of Y^{3+}, ζ-potential measurements were conducted on colloidal formulations that showed a loading percentage higher than 30% and the values are reported in Table S6 in the Supporting Information. Comparison of the
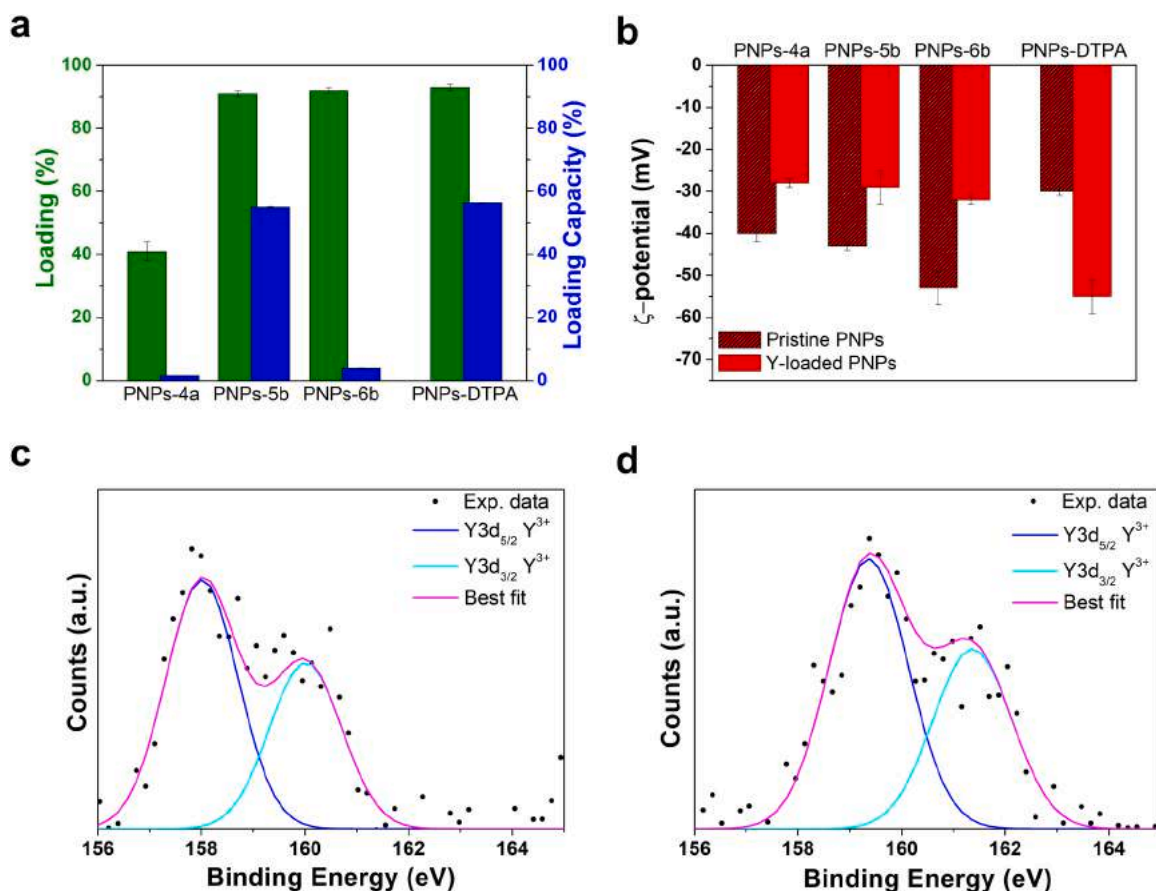
Fig. 4. (**a**) Loading percentage and loading capacity for PNPs loaded with PNPs/YCl₃ 10/1 wt ratio and 1.2 mg/mL YCl₃ stock solution. (**b**) ζ-potential trend before and after Y^{3+} loading on PNPs (PNPs/YCl₃ 10/1 wt ratio and 1.2 mg/mL YCl₃ stock solution). (**c**) XPS spectrum of p(MMA-co-DMAA)-Y and (**d**) XPS spectrum of p(MMA-co-AA)-DTPA-Y recorded at Y3d core level.

ζ-potential values before and after loading are shown in Fig. 4(b). As it can be seen, the ζ-potential values decrease after Y^{3+} loading in all p(MMA-co-DMAA)-Y samples. These results suggested the presence of positively charged yttrium ions interacting with the negatively charged surface of PNPs, thereby reducing the absolute value of the ζ-potential. Despite the high loading percentage $(93 \pm 1)\%$, an increase in the ζ-potential value for p(MMA-co-AA)-DTPA-Y formulation is evidenced. It is worthy to note that the loaded PNPs maintain good colloidal stability after the interaction with YCl₃ salt (–30 ≤ ζ-potential ≤ +30 is

taken as reference for stable suspension [51]), with repulsion between the nanobeads preventing their aggregation, in aqueous medium.

Qualitative detection of Y^{3+} was obtained *via* XPS measurements that allowed to probe YCl₃ on the surface of both p(MMA-co-DMAA)-Y NPs (MMA:DMAA 10:1, reaction time 2 h) NPs and p(MMA-co-AA)-DTPA-Y NPs. XPS spectra were collected at C1s, N1s, O1s, and Y3d (all BE (eV), FWHM (eV), relative intensity values and proposed signals assignments are reported in Table S3 in the Supporting Information). XPS spectra at C1s, N1s, O1s, core level of p(MMA-co-DMAA)-Y NPs and p(MMA-co-
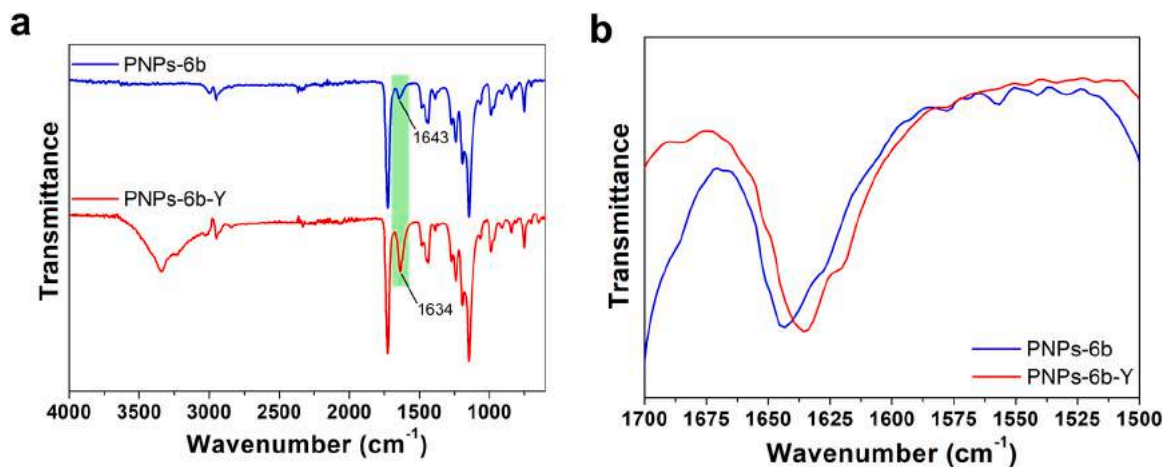

Fig. 5. a) FTIR spectrum recorded in ATR mode on PNPs-6a before (blue line) and after (PNPs-6b-Y, red line) yttrium loading. b) Magnification in the 1700–1500 cm⁻¹ region. Spectra were recorded on solid samples.

AA)-DTPA-Y NPs are reported in Fig. S9 in the Supporting Information. Y3d spectra in Fig. 4(c,d) are made of one spin-orbit pair, of which the Y3d$_{5/2}$ signal is taken as reference (Y3d$_{5/2}$ *ca.* 159.0 eV), that can be associated to the presence of Y^{3+} ions, interacting with DMAA (BE=158.0 eV) in the first case (Fig. 4(c)) and with DTPA chelating agent on PNPs (BE=159.6 eV) in the second sample (Fig. 4(d)). These results confirmed the loading of Y^{3+} ions on the PNPs surface.

Structural FTIR-ATR analysis to prove yttrium ions interaction with nanoparticles surface were performed on **PNPs-6b-Y** (MMA:DMAA 14:1, reaction time 4 h with %loading 92 ± 1%. Fig. 5 shows a comparison between pristine (unloaded) NPs and yttrium-loaded NPs Yttrium (III) chloride hexahydrate absorptions can be found in the range of 50–600 cm^{-1} [52] with vibrations in the 4000–600 cm^{-1} (Fig. S10) associated with water molecules of the hydrated salt (3200 cm^{-1} and
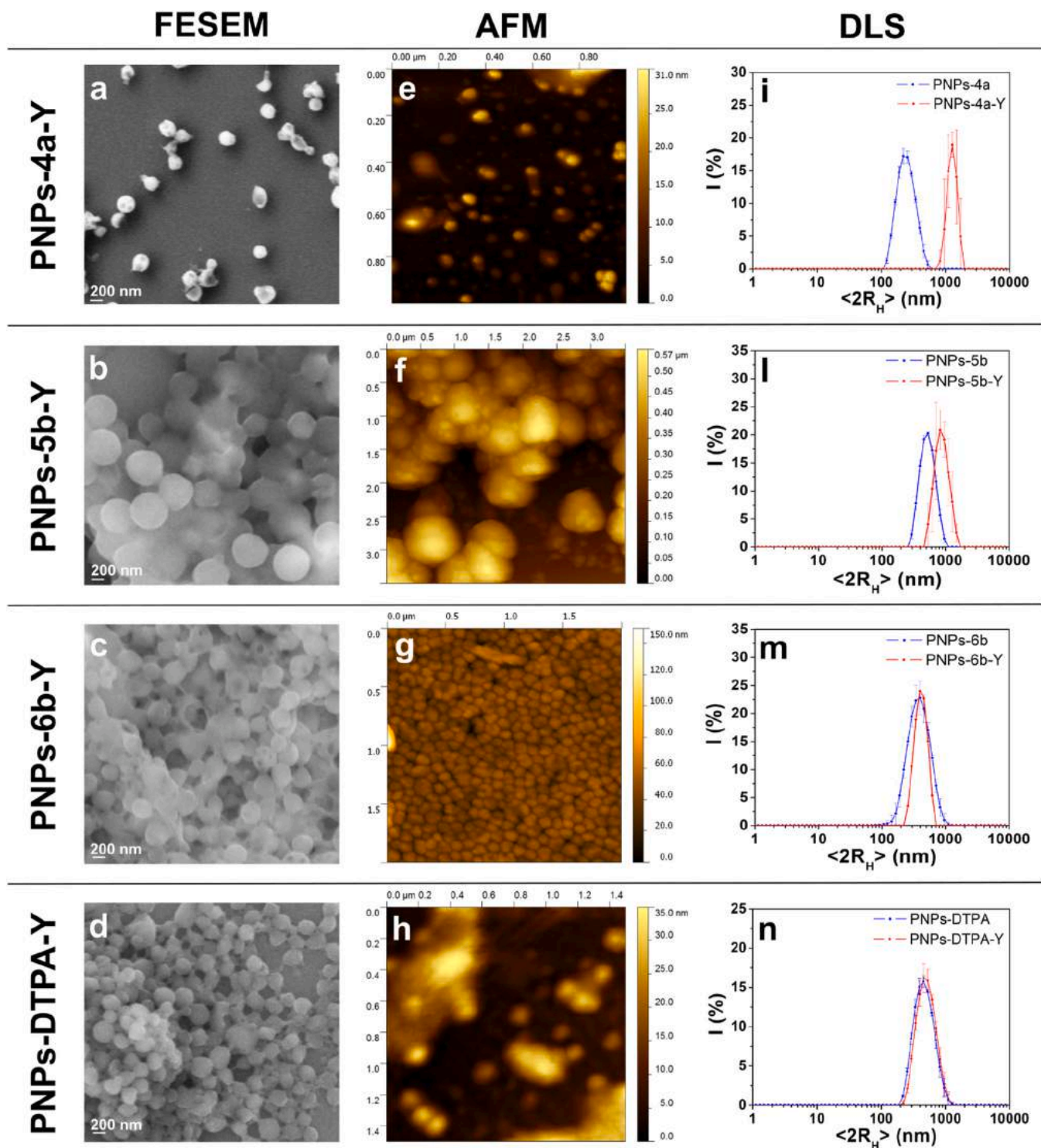

Fig. 6. PNPs characterization before and after loading with YCl$_3$: (**a-d**) FESEM images of PNPs-Y. (**e-h**) AFM images recorded on PNPs loaded with Y^{3+} ions. (**i-n**) DLS analysis (H$_2$O, 25 °C) of PNPs-4a, PNPs-5b, PNPs-6b and PNPs-DTPA. PNPs-4a $<2R_H> = 220 ± 90$ nm; PNPs-4a-Y $<2R_H> = 1280 ± 250$; PNPs-5b $<2R_H> = 530 ± 110$ nm; PNPs-5b-Y $<2R_H> = 955 ± 175$; PNPs-6b $<2R_H> = 395 ± 125$ nm; PNPs-6b-Y $<2R_H> = 430 ± 100$; PNPs-DTPA $<2R_H> = 483 ± 42$ nm; PNPs-DTPA-Y $<2R_H> = 499 ± 146$ nm.

1620 cm^{-1}). For pristine PNPs-6b (Fig. 5(a,b), blue line), the characteristic stretching vibrations of co-polymer appeared at 1727 cm^{-1} (C=O group of methylmethacrylate ester) and at 1643 cm^{-1} (C=O group of *N,N*-dimethylacrylamide), respectively. For yttrium-loaded nanoparticles (Fig. 5(a,b), red line), the same stretching vibrations are observed at 1727 cm^{-1} and 1634 cm^{-1}, with *ca.* 10 cm^{-1} redshift of the C=O band of amide groups. Thus, the coordination reaction with YCl$_3$ mainly involved the amide groups of DMAA with little to no observable interaction with MMA ester groups. A similar behavior was observed for Eu^{3+}- and Tb^{3+}-based coordination complexes with *poly*(*N*-isopropyl, *N*-methylacrylamide-*stat-N,N*-dimethylacrylamide) copolymer [34]. The redshift is associated with a weak C=O bond, *i.e.*, weak force constant, after complex formation due to oxygen lone pair interaction with yttrium orbitals [34].

The surface morphology, size, and stability after loading with Y^{3+} were analyzed by FESEM, AFM and DLS, respectively. Fig. 6 shows selected DLS measurements, FESEM, and AFM images of Y^{3+}-loaded nanoparticles: **PNPs-4a-Y** (%loading = 41 ± 3%), **PNPs-5b-Y** (% loading = 91 ± 1%), **PNPs-6b-Y** (%loading = 92 ± 1%) and **PNPs-DTPA-Y** (%loading = 93 ± 1%). In the FESEM images (Fig. 6(a-d)), Y^{3+}-loaded nanoparticles maintain their spherical shape and low polydispersity compared with the pristine samples (see Fig. 2). The NPs sizes by FESEM increased after the loading, which was consistent with the DLS results (Fig. 6(i-n)). AFM images (Fig. 6(e-h)) showed spherical-shaped nanobeads with a relatively smooth surface. It is noteworthy that for sample PNPs-4a-Y, a single population is observed in both FESEM and DLS analyses; the hydrodynamic diameter increases but at the solid-state individual nanoparticles were observed, with limited

aggregation and size remain comparable with unloaded pristine polymers. The compositional analysis and EDS mapping conducted on **PNPs-4a-Y** point out the presence of yttrium on the nanobeads surface (Fig. S11 in the Supporting Information).

4.5. Release studies

The release of yttrium ions in solution was studied. Y^{3+}-loaded nanoparticles (0.24 mg/mL) were dispersed in H$_2$O$_{up}$ at pH = 7.0 and 37 °C. The release was followed for both p(MMA-co-DMAA)-Y NPs (sample **PNPs-5b**, loading 92 ± 1%) and p(MMA-co-AA)-DTPA-Y NPs (loading 93 ± 1%), from 0 to 30 days and the data of cumulative drug release are shown in Fig. S12 in the Supporting Information. Within the first day, release was evaluated in the 0–5-hour range. After 1 h, the release reached the cumulative values of (11.7 ± 0.1)% and (12.9 ± 0.2)% for p(MMA-co-DMAA)-Y and p(MMA-co-AA)-DTPA-Y, respectively. Then, the release settles to a constant value of (12 ± 3)% and (11 ± 1)% over a month.

4.6. Stability studies in water and culture medium

According to the morphological and structural characterizations, **PNPs-4a**, **PNPs-4a-Y**, **PNPs-DTPA**, and **PNPs-DTPA-Y** were selected as representative samples for stability tests. Before biological assays, the colloidal stability of the as-prepared NPs in both H$_2$O$_{up}$ and RMPI-1640 (supplemented with 10% FBS) culture medium was evaluated by DLS and SAXS (Fig. 7). Stability studies were extended to p(MMA-co-AA)-DTPA and p(MMA-co-AA)-DTPA-Y to evaluate the response of each
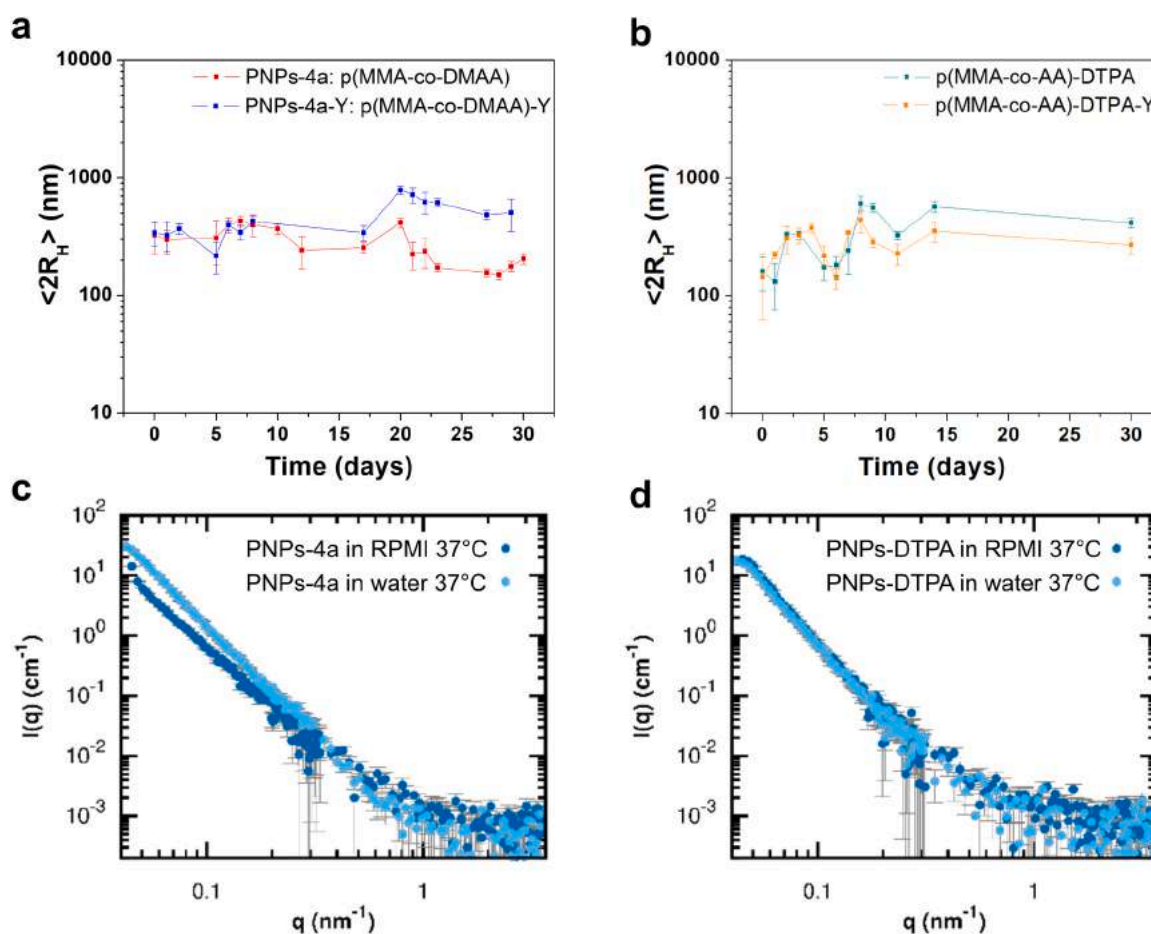

Fig. 7. Stability evaluated by DLS of (**a**) p(MMA-co-DMAA) PNPs-4a formulations and (**b**) p(MMA-co-AA) formulations in RPMI-1640 (10% FBS) at 37 °C. (**c**) Comparison of experimental SAXS profiles of p(MMA-co-DMAA) PNPs-4a suspensions (1.4 mg/mL) in RPMI medium and water at 37 °C. (**d**) Comparison of experimental SAXS profiles of p(MMA-co-AA)-DTPA NPs suspensions (14.2 mg/mL) in RPMI medium and water at 37 °C.

formulation. To do so, 0.1 mg of PNPs solid pellet were added to 1 mL of RPMI-1640 culture medium to obtaining a nano-formulation at concentration 0.1 mg/mL. At prescriptive intervals within 30 days, the particle size was measured by DLS at 37 °C. Copolymeric p(MMA-co-DMAA) (**PNPs-4a**, MMA:DMAA 10:1, 2 h) remain quite stable over 30 days, indicating that the interaction with serum proteins or the presence of salts and vitamins did not alter their colloidal stability (Fig. 7(a)). However, increase in the hydrodynamic diameter from (400 ± 80) nm to (785 ± 65) nm occurs in the loaded sample after 20 days. For p(MMA-co-AA)-DTPA formulations (Fig. 7(b)) no significant changes were detected within 6 days in RPMI-1640, although aggregation occurs after 1 week in both pristine and loaded samples. To obtain further details about stability, SAXS measurements were performed at different time points (within 24 h) and environments, *i.e.*, water and RPMI-1640 complete medium, at T = 37 °C. The SAXS profile of p(MMA-co-DMAA) (**PNPs-4a**, 1.4 mg/mL) and p(MMA-co-AA)-DTPA (14.2 mg/mL) recorded at different time points is reported in Fig. S13 in the Supporting Information. The SAXS profiles collected on both polymeric nanoparticles suspensions within 24 h (Fig. 7(c,d)) are in agreement with particle radii of the order of 200 nm, and therefore beyond the limits for a reliable size evaluation within the available angular range $(q_{min}\ 0.045\ nm^{-1},\ D_{max}\sim70\ nm)$. Considering the acquisition time of 24 h for the samples dispersed in the RPMI-1640 medium (the same environment used for next *in vitro* experiments) or ultrapure water at 37 °C, we can assess the colloidal stability. Comparing DLS and SAXS results we can infer that the synthetic approach successfully produced nanobeads with morpho-colloidal stability in different media, *i.e.*, ultrapure water, RPMI-1640 culture medium, over 24 h at 37 °C, although for pristine p(MMA-co-DMAA) NPs a better colloidal stability was obtained within 30 days. Considering prolonged period of time, yttrium loading partially affect colloidal stability of polymeric nanoparticles, being **PNPs-4a-Y** the most stable colloids compared with p(MMA-co-AA)-DTPA-Y.

4.7. Swelling properties of polymeric nanoparticles

Swelling behavior of polymeric nanoparticles was evaluated *via* dynamic light scattering. Two different conditions were studied (i) different water-miscible solvents: methanol, ethanol, and ethylene glycol, and (ii) swelling in water at different pHs (3−11). For the tests, PNPs-6b (MMA:DMAA 14:1, 4 h) was taken as representative sample.

Fig. 8(a) shows the hydrodynamic size distribution of polymeric nanoparticles in different environments. Compared with pristine PNPs-6b in water ($<2R_H> = 395 \pm 125$ nm), the hydrodynamic size tends to decrease in both methanol ($<2R_H> = 295 \pm 75$ nm) and ethanol ($<2R_H> = 223 \pm 19$ nm), whereas an increase in the $< 2R_H> = 531$

$\pm$ 168 nm occurs in ethylene glycol. The solvent-induced deswelling of polymeric nanoparticles in methanol and ethanol compared with ethylene glycol can be explained in terms of solubility parameters [53,54]. Methanol and ethanol act as water-miscible non-solvent for methylmethacrylate-based polymeric nanoparticles, causing a collapse of the nanostructured polymeric envelope [53]. Solvent-induced swelling appears in ethylene glycol, driven by proximity of solubility parameters between the polymer and the solvent [54].

The influence of pHs on PNPs-6b swelling was also investigated. Fig. 8(b) shows the mean hydrodynamic diameter of the nanoparticles *versus* the pH of the medium. The hydrodynamic diameter of polymeric nanoparticles showed a clear tendency to decrease when pH moved from 3 to 11. This deswelling can be explained based on the anionic behavior of p(MMA-co-DMAA) polymer, as resulted from ζ-potential value of -53 ± 4 mV. The lowering of the pH value below 7 led to a transition from charged to uncharged nanoparticles, with subsequent change in the size and size distribution due to aggregation phenomena [55]. Conversely, at neutral and basic pHs (above 7) nanoparticles were stabilized by electrostatic repulsion, leading to almost identical swelling degree. Complete DLS size distributions are reported in Fig. S14.

4.8. PNPs cytocompatibility evaluation and TEM studies

In order to achieve clinical impacts for applications in nanomedicine, systemic *in vitro* studies were performed to obtain insight into cytocompatibility of the as-prepared formulations. *In vitro* evaluation allows to analyze the acute harmful effects of polymeric nanoparticles in a specific cellular environment; although *in vitro* studies does not replace the *in vivo* evaluation through which the biodistribution is studied with animal models. Cytotoxicity studies allowed to investigate the effects of the nanoparticles on cell adhesion and cell survival under a controlled environment. Controlled growth conditions reduce the uncertainties in experimental measurements by increasing the reliability of the data obtained. In this study, glioblastoma cell line T98G was used to test toxicity of the as-synthesized nanobeads of different chemical composition and at different concentrations, *i.e.*, 10 μg/mL, 30 μg/mL, and 50 μg/mL. To exclude cytotoxic effect of DTPA chelating agent functionalizing the p(MMA-co-AA)-DTPA surface, *in vitro* experiments were performed also on non-functionalized p(MMA-co-AA), as a comparison. The effect on colony forming capacity, *i.e.*, cell survival, after 24 h of exposure of cells to nanobeads was evaluated. The results of the toxicity assay for the three types of NPs: pristine p(MMA-co-AA) (reported as **PNPs-AA**), **PNPs-DTPA** and **PNPs-DTPA-Y**, evaluated in terms of survival are shown in Fig. 9. Compared to the control (cells not treated with the NPs) the survival of cells treated with pristine **PNPs-AA** appears to
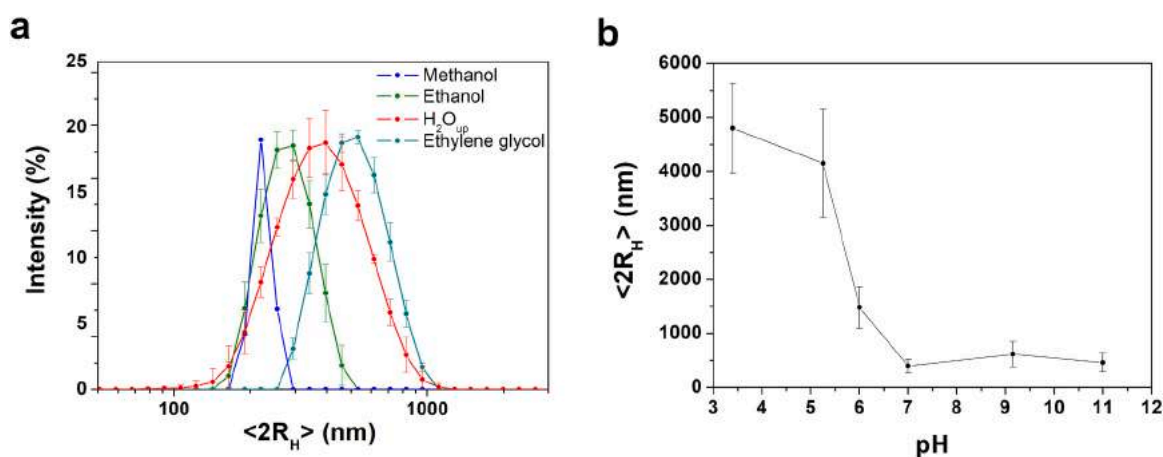

Fig. 8. a) DLS measurements on PNPs-6b in different solvents: methanol (blue line), ethanol (green line), water (red line), and ethylene glycol (dark cyan line). b) Mean hydrodynamic diameter value as a function of pH of PNPs-6b.
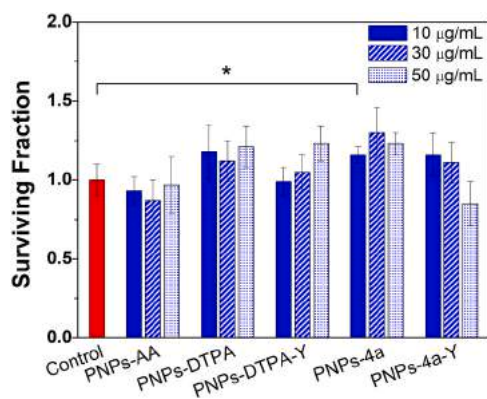
Fig. 9. Surviving Fraction (S.F.) In vitro biological studies on T98G cell line treated with p(MMA-co-AA) NPs and p(MMA-co-DMAA) (PNPs-4a) formulations with and without Y^{3+} loading at different concentrations: 10 µg/mL (plain bars), 30 µg/mL (bars with medium pattern), and 50 µg/mL (bars with dense pattern). Asterisk (*) denotes significant difference from the control group (p < 0.05).

decrease for all three tested concentrations; while the survival of cells treated with **PNPs-DTPA** appears to increase for all three tested concentrations. However, the differences between both concentrations and the two types of NPs were not statistically significant. A different trend is observed for the survival of cells treated with the **PNPs-DTPA-Y**, which increases as the concentration increases, but again there is no statistical significance. The results of the toxicity assay for the other p(MMA-co-DMAA) NPs (unloaded **PNPs-4a** and **PNPs-4a-Y**) evaluated in terms of survival are shown in Fig. 9. Compared to the control the survival of cells treated with PNPs appears to increase with increasing concentration up to 30 µg/mL and then decrease at the concentration of 50 µg/mL. The differences observed between the various concentrations are not statistically significant while a statistically difference (p < 0.05) is observed with respect to control at the lowest concentration. A different trend is observed for the survival of cells treated with **PNPs-4a-Y**, which seems to decrease as the concentration increases, but again there is no statistical significance, either between concentrations or with respect to control. These results demonstrated the non-cytotoxic effect within 24 h treatment of the PNPs among the concentration range explored.

Two synthesized species of hydrated nanoparticle polymers both loaded with yttrium ions were able to cross cell membrane of human glioblastoma T98G cells, as a model cancer cell line. Direct imaging TEM observations confirms the potential ability of the PNPs to be well sequestered by cancer cells (T98G@**PNPs-4a-Y** 50 µg/mL and T98G@**PNPs-DTPA-Y** 50 µg/mL, Fig. 10). Anchoring **PNPs-4a-Y** aggregates during cellular internalization are clearly visible in the Fig. 10 (a-d), which are approaching to the membrane surface to be uptake by endocytic pathways. The first approach of a large **PNPs-4a-Y** cluster of 1.5×2.5 µm^2 in size to the cell shows a shape change of the membrane surface for binding the inert PNPs by forming an initial protrusion extension of the membrane to wrap them (Fig. 10a). Similarly, a presence of a nonspecific cellular uptake route can be observed in Fig. 10(b), a typical macropinocytosis pathway characterized by nonspecific internalization, resulting in anchoring **PNPs-4a-Y** aggregate (1.1×1.6 µm^2) *via* cell membrane ruffling (protrusion extension). A phagocytosis pathway is also evident through the outward membrane protrusions that hug large **PNPs-4a-Y** aggregate (1.6×2.1 µm^2); while protruding pseudopod mechanism also occurred for relatively small PNPs aggregate (0.8×0.9 µm^2) with the formation of a phagocytic cup around the particle target, as shown in Fig. 10(c,d). The resulting internalized **PNPs-4a-Y**, mainly through phagocytosis/macropinocytosis pathways, can be observed (blue dot line square in Fig. 10 (e). Few **PNPs-4a-Y** entrapped into endocytic vesicles that were actively transported by molecular motors towards the perinuclear region is

displayed in the magnified image of Fig. 10(f).

Interestingly, further TEM observations evidenced nanometric **PNPs-4a-Y** not-aggregated without extension in membrane protrusions, which preserved their spherical shape either when they were not attached to the cell membrane and during either binding to the cell membrane and internalized by phagocytosis, a possible stiffer nanoparticle (white arrows, Fig. 10(g). Furthermore, a possible soft PNPs displayed substantial deformations during both binding and internalization (blue arrows, Fig. 10(g)) [56].

Further evidence of the phagocytosis pathway may be observed in Fig. 10(h), wherein the smallest **PNPs-4a-Y** cluster (0.5×0.6 µm^2) is anchored on the membrane surface. One more small aggregate (500 nm) was sequestered in a clear endocytic vesicle with the presence of biological fluids in the range of a few hundreds of nanometres (green dot line square, Fig. 10(i)). Therefore, micrometric aggregates and single nanometric **PNPs-4a-Y** are both internalized efficiently and have higher uptake pathways, following different endocytic mechanisms.

Cellular internalization of T98G@**PNPs-DTPA-Y** aggregates is shown on the bottom display item of Fig. 10. Similarly, the membrane surface evidences an adaptation to the surrounding microenvironment by following the spherical shape of the **PNPs-DTPA-Y** cluster of about 500 nm (Fig. 10a′). An early phase of the macropinocytosis process can be observed in Fig. 10(b′-d′); wherein a morphological change of pseudopod extensions surrounding the **PNPs-DTPA-Y** microaggregates target can be noticed. **PNPs-DTPA-Y** aggregate internalized near the perinuclear region is displayed in Fig. 10(e′) (blue dot line square). The magnified image of Fig. 10(f′) evidence **PNPs-DTPA-Y** densely packed aggregate and a single PNP.

By imaging observations of the endocytic and internalizations mechanisms, T98G@ **PNPs-4a-Y** well sequestered by cancer cells showing both phagocytosis/macropinocytosis pathways with further evidence of not-aggregate PNPs anchored and internalized without ruffled membrane extension. Besides, imaging observations of T98G@**PNPs-DTPA-Y** still clearly showed uptake of the PNPs, following mainly macropinocytosis pathway. Furthermore, the membrane surfaces of the cells exhibit a U-shaped feature, mimicking all PNPs aggregates independently from their surface shape during the anchoring phase.

Further observations of the alone **PNPs-4a-Y** are displayed in Fig. 10 (g′), showing polymeric nanoparticles with a spherical shape of 230 nm, confirming the previous morphology findings. An electron diffraction measurement has been probed on the PNPs to study eventually structural organization (orange dot line circle). A weak signal of the electron diffraction pattern (EDP) is shown in Fig. 10(h)', indicating the presence of nanocrystal randomly oriented characterized by typical diffraction rings. By measuring the D-spacing of the diffraction rings, we were able to characterize the EDP belonging to the nanocrystals molecule of hexaaquadichloroyttrium(lll)chloride ([YCl$_2$(H$_2$O)$_6$]Cl) structure; wherein the yttrium is coordinated by two chlorines and six water molecules in a square antiprismatic arrangement [57]. The calculated D-spacing of a space group P 1 2/n 1 well matched with our experimental diffraction rings (by blue line arcs), in which the measured and calculated relative intense signal belongs to the (100) diffraction plane of $d_{101} = 0.585$ nm. The resulting identified diffraction planes have different crystalline orientations; thereby, the molecular nanocrystals have no preferential orientation, probably due to their chemical localized position on the PNPs surface. The hydrated **PNPs-4a-Y** treated with the same procedure of the cells (Section 2.9) embedded in an epoxydic resin exhibit a quasi-core-shell character with different diameters, depending on the height of the cross-section (Fig. 10(i′)). It should be noted that the pristine nanoparticles preserve their spherical shape while they change shape in polyhedral during their cancer cell interactions (*e.g.*, Figs. 10 (b),10(i), 10(a′), *etc.*).

Surface electron imaging observations were performed on hydrated human glioblastoma T98G cells before and after PNPs treatment in order to provide further evidence of the non-cytotoxic effect of the PNPs
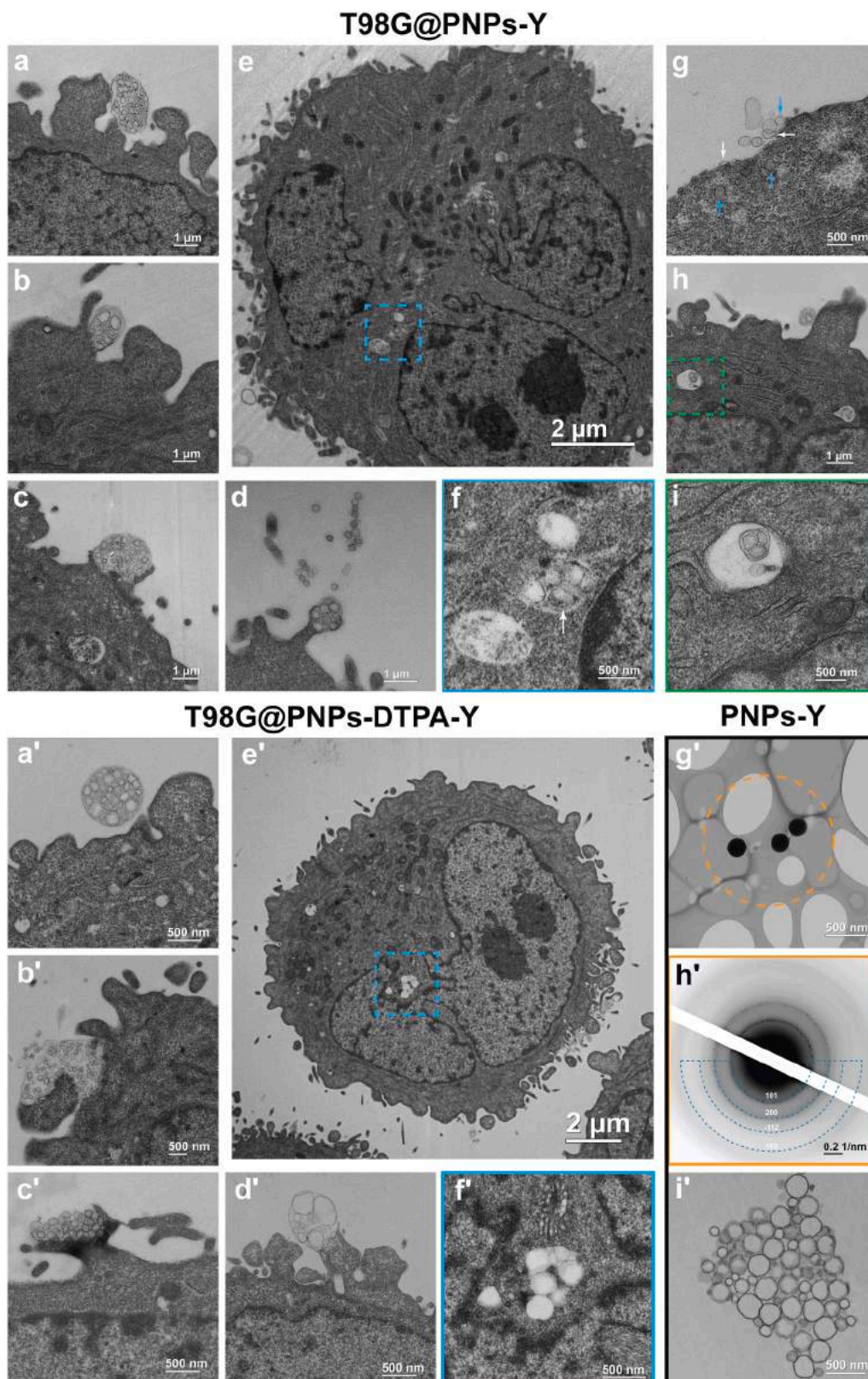
Fig. 10. Morphostructural observations of PNPs uptake by human glioblastoma (T98G) cells. (**a-d**) T98G@PNPs-4a-Y 50 µg/mL aggregates anchoring by endocytic pathways. (**e**) Cross-section of T98G cell with smallest PNPs aggregate internalized near perinuclear region (blue dot line square) and (**f**) the corresponding magnified area. (**g**) Not-aggregate PNPs interacting with the membrane surface. (**h**) PNPs in early and after internalizations and the corresponding magnified area (green dot line square). (**a′-d′**) T98G@PNP-DTPA-Y 50 µg/mL aggregates uptake by endocytic pathways. (**e′**) Cross-section of T98G cell with smallest PNPs aggregates internalized near perinuclear region (blue dot line square) and (**f′**) the corresponding magnified area. (**g′**) Alone PNPs and (**h′**) the corresponding electron diffraction pattern. (**i′**) Pristine PNPs-4a-Y embedded in an epoxydic resin.

(T98G cells after incubation with PNPs are herein indicated as T98G@PNPs). VP-SEM of untreated control, *i.e.*, T98G cells, are reported in Fig. S15 in the Supporting Information. As can be observed from VP-SEM images, the control cells showed the typical morphology of elongated, flat, and well spread with small filopodia, suggesting cell motility. The presence of rounded-shaped cells is due mitosis process. After 24 h of incubation of T98G cells with both PNPs formulations (**PNPs-4a-Y** and **PNPs-DTPA-Y**), cells did not show significance differences compared with the untreated control (Fig. S16 in the Supporting Information).

4.9. Dye-encapsulated PNPs and fluorescence microscopy measurements

FITC-encapsulated PNPs, *i.e.*, p(MMA-co-DMAA)/FITC NPs (here denoted as **PNPs-F**) and p(MMA-co-AA)-DTPA/FITC NPs (here denoted as **PNPs-DTPA-F**) were synthesized to obtain fluorescent polymeric nanoparticles to be used as optical imaging agents. According to the structural and morphological characterizations of non-fluorescent PNPs discussed in Sections 4.2 and 4.3, two types of formulations were selected, *i.e.*, p(MMA-co-DMAA) NPs with MMA/DMAA 10/1 molar ratio and p(MMA-co-AA)-DTPA NPs with MMA:AA 12:1 molar ratio. FITC (3.33 mg/mL dissolved in acetone before use) was added to the mixture of the two comonomers. Then, the synthesis was accomplished following the procedure described in Section 2.6. To demonstrate the acquired optical feature due to dye loading, UV-Vis spectra on both pristine and dye-encapsulated PNPs were recorded (Fig. 11). Spectroscopic measurements were carried out in water (where the nanostructure maintain its stability) and chloroform (that dissolve the nanostructure causing the release of the encapsulated species). Thus, this approach is useful to evaluate the entrapment efficacy of different molecules inside the PNPs core. From Fig. 11(a,b), the absorbance

spectra for both **PNPs-F** and **PNPs-DTPA-F** showed the typical scattering phenomena due to colloidal nature of PNPs, with little-to-no absorption of FITC dye in the 400–500 nm wavelength region. In chloroform (red line in Fig. 11(a,b)), it is interesting to observe that the absorption of the FITC dye at $\lambda_{max} = 450$ nm drastically increases proving the effective encapsulation of the dye inside PNPs core. For comparison, the UV-Vis spectrum of pure FITC in water at pH = 11 is reported in Fig. S17 in the Supporting Information. Hydrodynamic diameter, polydispersity index, and ζ-potential of the obtained colloids were measured by DLS in H_2O_{up} at 25 °C. In the FITC-encapsulated p(MMA-co-DMAA) formulation the measured $< 2R_H >$ value was 285 ± 105 nm (PDI 0.133). The slight increase in size of the **PNPs-F**, as compared to pristine PNPs ($<2R_H> = 220 \pm 90$ nm), was ascribed to the loading of the dye (Fig. 11c). Size of the pure p(MMA-co-AA)-DTPA NPs and **PNPs-DTPA-F** were accounted to be (483 ± 42) nm and (322 ± 95) nm with PDI of 0.143 and 0.234, respectively (Fig. 11d). Despite the volume contraction in **PNPs-DTPA-F**, a higher polydispersity index was detected. Moreover, the ζ-potential of the nanoparticles was found to be (–30 ± 6) mV and (–27 ± 2) mV for **PNPs-F** and **PNPs-DTPA-F**, respectively. The dye-encapsulated NPs showed similar ζ-potential values compared with pristine PNPs, *i.e.*, (–40 ± 2) mV and (–30 ± 1) mV for p(MMA-co-DMAA) and p(MMA-co-AA)-DTPA, respectively, thus demonstrating that the entrapment of the dye inside the PNPs core did not affect the colloidal stability. Accurate structural characterizations were from FTIR and XPS. In the FTIR-ATR spectrum of pure FITC (Fig. S17), a broad band at about 3000 cm^{-1} associated with $\nu(-OH)$, and a strong $-N=C=S$ characteristic stretching vibration at 2046 cm^{-1} as well as signal at a 1733 cm^{-1} assigned to the carbonyl group of the lactone can be seen. Furthermore, the absorption peaks at 1591, 1541, and 1453 cm^{-1} were characteristics of benzene ring C=C-C stretching vibrations.
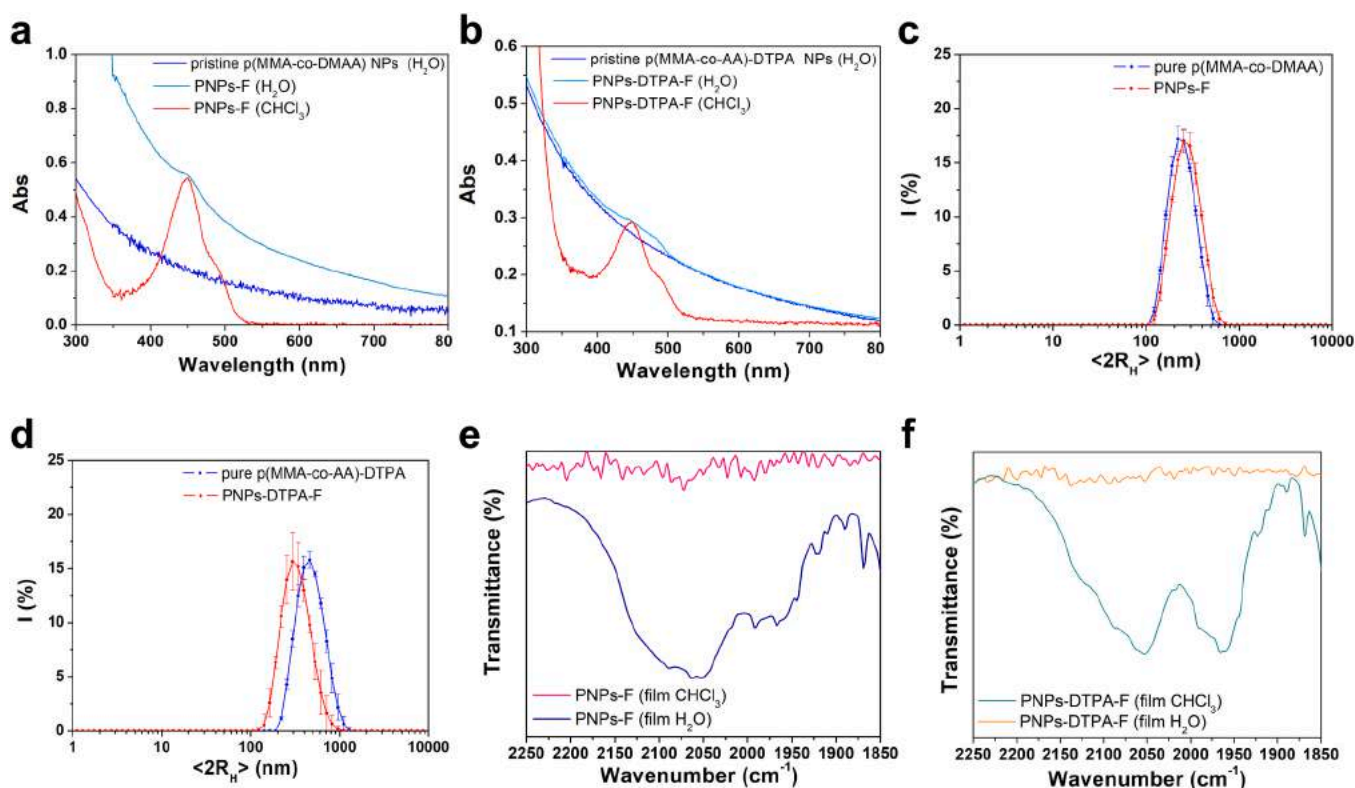

Fig. 11. (**a**) UV-Vis spectra of pristine p(MMA-co-DMAA) NPs (blue line), FITC-encapsulated NPs in H_2O (light blue line) and chloroform (red line). (**b**) UV-Vis spectra of pristine p(MMA-co-AA)-DTPA NPs (blue line), FITC-encapsulated NPs in H_2O (light blue line) and chloroform (red line). (**c**) DLS size distribution of pristine p(MMA-co-DMAA) NPs (blue line) and PNPs-F (red line). (**d**) DLS size distribution of pristine p(MMA-co-AA)-DTPA NPs (blue line) and PNPs-DTPA-F (red line). (**e**) Superimposition of FTIR-ATR spectra PNPs-F deposited from CHCl$_3$ and H_2O in the 2250–1850 cm^{-1} region. (**f**) Superimposition of FTIR-ATR spectra of PNPs-DTPA-F deposited from CHCl$_3$ and H_2O in the 2250–1850 cm^{-1} region.

For **PNPs-F** deposited from the aqueous solution (blue line in Fig. 11e), FTIR spectrum reported in the 2250–1850 cm^{-1} wavenumber region showed no signals associated to the presence of FITC. Deposition from chloroform suspension (known to disrupt the nanostructure) of the same sample (pink line in Fig. 11(e)) revealed the presence of broad bands centered at 2050 cm^{-1} and at 3444 cm^{-1}, due to $\nu(-N=C{=}S)$ and $\nu(-OH$ carboxylic group) of the encapsulated fluorescein inside the core of polymeric nanoparticles. Complete p(MMA-co-DMAA)/FITC NPs spectra are reported in Fig. S18 in the Supporting Information. In the FTIR-ATR spectrum of **PNPs-DTPA-F** (2250–1850 cm^{-1} range) deposited from water (orange line in Fig. 11(f)), compared with pristine FITC, the isothiocyanate stretching vibration is absent, whereas a weak band centered at about 2060 cm^{-1} can be found in the spectrum recorded on the sample deposited from CHCl$_3$ suspension (dark cyan line in Fig. 11 (f)). Complete p(MMA-co-AA)-DTPA/FITC NPs spectra are reported in Fig. S18 in the Supporting Information.

XPS measurements were also performed on FITC-encapsulated nanobeads deposited on TiO$_2$ substrate, *i.e.*, p(MMA-co-DMAA)/FITC NPs and p(MMA-co-AA)-DTPA/FITC NPs, to obtain a better insight into the dye molecular structure stability upon encapsulation inside NPs. Measurements were performed on the C1s, N1s, O1s and S2p core levels. All binding energy (BE) values, FWHM and atomic ratios are reported in Table S2 in the Supporting Information. The measured C1s and S2p core level spectra confirmed the stability of the FITC molecular structure in both formulations (Fig. S19 in the Supporting Information). C1s signal appeared composite and applying a peak-fitting procedure at least four components can be identified corresponding to: (i) C atoms bonded to other carbons in aromatic molecules (aromatic C−C), (ii) aliphatic C

atoms (aliphatic C−C) (BE = 284.7 eV), (iii) C atoms bonded to N in C−N and $-N=C{=}S$ group and (iv) C bonded to O in C−O (BE *ca.* 286.0 eV) and C=O groups (BE *ca.* 287.5 eV) and, at higher BE values, C atoms of the carboxyl group (BE *ca.* 289.0 eV). The S2p spectra showed three pairs of spin-orbit components. The first doublet, taken S2p$_{3/2}$ signal as reference for the S2p$_{3/2-1/2}$ spin−orbit pair (S2p$_{3/2}$ BE *ca.* 161.0 eV) appeared at BE values typical of sulfur atoms covalently bonded to carbon in isothiocyanate (R$-$N$=$C$=$S) moieties. Overall, UV-Visible and FTIR spectroscopies confirmed that the FITC molecules were successfully encapsulated inside the inner core of PNPs. Moreover, XPS allowed to assess that the encapsulation preserves the structural stability of the dye.

The encapsulation of FITC dye was confirmed by spectroscopic measurements and the strength of optical imaging was highlighted with fluorescence optical microscopy measurements. To validate the use of FITC-encapsulated PNPs as optical imaging probes, fluorescence microscopy studies were performed. Nanobeads containing the encapsulated fluorescent dye were deposited onto a glass microscope slide from their aqueous suspension and observed by fluorescence microscopy to evaluate the fluorescence intensity of each sample. Fig. 12(a,b) showed small-sized and quite homogeneous fluorescent **PNPs-F** in the 200–500 nm size range. Bright fluorescence was also recorded for **PNPs-DTPA-F** (Fig. 10(c,d)) although larger and more polydisperse NPs can be seen, as already measured by DLS (see Section 4.8). In both cases, the synthesis method allowed to obtain dye-encapsulated polymeric nanobeads. In addition, fluorescent nanobeads formulations did not show noticeable fluorescence quenching, with promising applications as optical imaging probes.
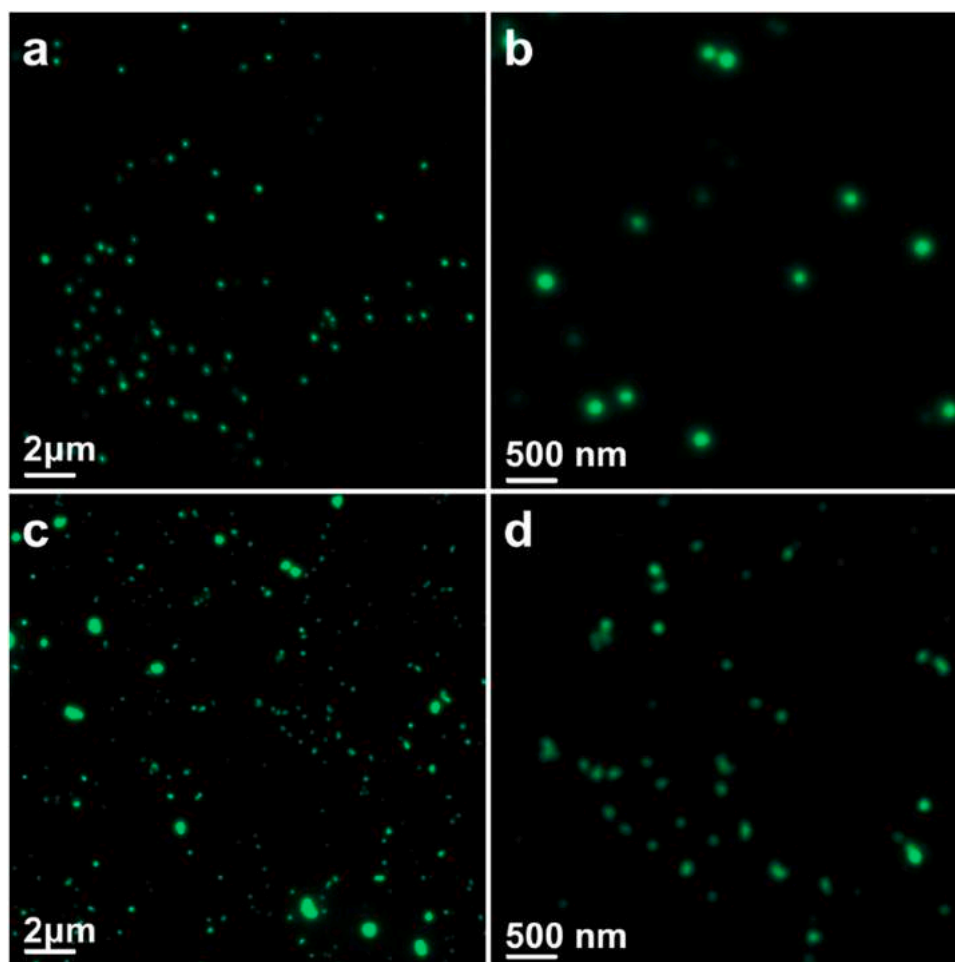

Fig. 12. Fluorescence microscopy images of (**a,b**) PNPs-F and (**c,d**) PNPs-DTPA-F.

5. Conclusions

Novel acrylate-based polymeric nanobeads, *i.e.*, p(MMA-co-DMAA), were successfully synthesized using a surfactant-free radical emulsion polymerization technique in presence of persulfates as radical initiators. First, optimization of the reaction conditions was done through modification of crucial synthesis parameters: (i) MMA:DMAA molar ratio (from 10:1–14:1); (ii) reaction time (2–4–6 h); (iii) temperature (70 °C or 80 °C). According to structural (FT-IR, ^{1}H and ^{13}C NMR, XPS) and morphological characterizations (FESEM, AFM, TEM), the best results in terms of size, polydispersity, stability (probed by DLS and SAXS over 30 days), and spherical morphology were obtained at 80 °C. Changes in polymeric nanoparticles dispersion medium and pH control the swelling behavior of the colloids. The higher degree of swelling was obtained in ethylene glycol compared with methanol and ethanol. Neutral and basic pH values (< 7) allowed to obtained better nanoparticles dispersion, due to electrostatic repulsion forces between polymeric chains that stabilize the nanobeads towards aggregation. In view of applications in nanomedicine, polymeric nanobeads were loaded with Y^{3+} ions achieving loading percentages of *ca.* 90% with high loading capacity. The coordination complex between polymeric nanoparticles and yttrium involved the amide group of DMAA co-monomer, as resulted from FT-IR measurements. A comparison with previously published p(MMA-co-AA)-DTPA NPs functionalized with DTPA chelating agent allowed to assess the chelation ability of p(MMA-co-DMAA) NPs towards Y^{3+} ions. *In vitro* studies on human glioblastoma multiforme T98G cell line revealed the absence of cytotoxicity within 24 h treatment. TEM observations of T98G cancer cells incubated with the nanoparticles confirmed an active uptake of PNPs through multiple endocytic pathways (phagocytosis/macropinocytosis) to final reach perinuclear region of the cell. Then, dye-encapsulated p(MMA-co-DMAA) nanoprobes were synthesized with physical encapsulation of the FITC isomer I dye inside the core of nanostructured polymers, as demonstrated by UV-Vis and FTIR measurements. Furthermore, structural integrity of the encapsulated FITC was confirmed by XPS and fluorescence microscopy analyses. As demonstrated, the possibility to immobilize yttrium ions on the surface of polymeric nanobeads and to encapsulate fluorescent molecules inside the inner core of nanoparticles, *i.e.*, FITC isomer I, opens new perspectives to develop nano-formulation for diagnostic (imaging) applications.

CRediT authorship contribution statement

Sara Cerra: Conceptualization, Investigation, Writing – original draft. **Valentina Dini**: Investigation. **Tommaso A. Salamone**: Visualization. **Farid Hajareh Haghighi**: Visualization. **Martina Mercurio**: Visualization. **Antonella Cartoni**: Conceptualization, Investigation. **Alessandra Del Giudice**: Investigation. **Martina Marsotto**: Investigation. **Iole Venditti**: Visualization. **Chiara Battocchio**: Investigation. **Francesca A. Scaramuzzo**: Investigation. **Roberto Matassa**: Investigation. **Stefania Nottola**: Visualization. **Riccardo Faccini**: Visualization. **Riccardo Mirabelli**: Visualization. **Ilaria Fratoddi**: Supervision, Conceptualization, Funding acquisition, Writing – review & editing.

Declaration of Competing Interest

The authors declare that they have no known competing financial interests or personal relationships that could have appeared to influence the work reported in this paper.

Data Availability

Data will be made available on request.

Appendix A. Supporting information

Supplementary data associated with this article can be found in the online version at doi:10.1016/j.colsurfa.2023.131829.

References

[1] D. Quesada-González, A. Merkoçi, Nanomaterial-based devices for point-of-care diagnostic applications, Chem. Soc. Rev. 47 (2018) 4697–4709, https://doi.org/10.1039/C7CS00837F.

[2] F. Albalawi, M.Z. Hussein, S. Fakurazi, M.J. Masarudin, Engineered nanomaterials: the challenges and opportunities for nanomedicines, Int. J. Nanomed. 16 (2021) 161–184, https://doi.org/10.2147/IJN.S288236.

[3] E. Calzoni, A. Cesaretti, A. Polchi, A. Di Michele, B. Tancini, C. Emiliani, Biocompatible polymer nanoparticles for drug delivery applications in cancer and neurodegenerative disorder therapies, J. Funct. Biomater. 10 (2019) 4, https://doi.org/10.3390/jfb10010004.

[4] Y. Qi, M. He, S. Long, W. Feng, H. Yana, Construction of hyperbranched polysiloxane-based multifunctional fluorescent prodrug for preferential cellular uptake and dual-responsive drug release, Biomater. Adv. 137 (2022), 212848, https://doi.org/10.1016/j.bioadv.2022.212848.

[5] J.-H. Jang, S.-H. Jeong, Y.-B. Lee, Preparation and in vitro/in vivo characterization of polymeric nanoparticles containing methotrexate to improve lymphatic delivery, Int. J. Mol. Sci. 20 (2019) 3312, https://doi.org/10.3390/ijms20133312.

[6] I. Schlachet, H.M. Halamish, A. Sosnik, Mixed amphiphilic polymeric nanoparticles of chitosan, poly(vinyl alcohol) and poly(methyl methacrylate) for intranasal drug delivery: a preliminary in vivo study, Molecules 25 (2020) 4496, https://doi.org/10.3390/molecules25194496.

[7] L. Dai, C.-L. Si, Cellulose-graft-poly(methyl methacrylate) nanoparticles with high biocompatibility for hydrophobic anti-cancer drug delivery, Mater. Lett. 207 (2017) 213–216, https://doi.org/10.1016/j.matlet.2017.07.090.

[8] E. Niza, A. Ocaña, J.A. Castro-Osma, I. Bravo, C. Alonso-Moreno, Polyester polymeric nanoparticles as platforms in the development of novel nanomedicines for cancer treatment, Cancers 13 (2021) 3387, https://doi.org/10.3390/cancers13143387.

[9] S. Sur, A. Rathore, V. Dave, K.R. Reddy, R.S. Chouhan, V. Sadhu, Recent developments in functionalized polymer nanoparticles for efficient drug delivery system, Nano-Struct. Nano-Objects 20 (2019), 100397, https://doi.org/10.1016/j.nanoso.2019.100397.

[10] A. Czajka, P.A. Lovell, S.P. Armes, Time-resolved small-angle X-ray scattering studies during the aqueous emulsion polymerization of methyl methacrylate, Macromolecules 55 (2022) 10188–10196, https://doi.org/10.1021/acs.macromol.2c01801.

[11] W. Yang, B. Xia, L. Wang, S. Ma, H. Liang, D. Wang, J. Huang, Shape effects of gold nanoparticles in photothermal cancer therapy, Mater, Today Sust. 13 (2021), 100078, https://doi.org/10.1016/j.mtsust.2021.100078.

[12] I. Venditti, A. Cartoni, L. Fontana, G. Testa, F.A. Scaramuzzo, R. Faccini, C. Mancini Terracciano, E. Solfaroli Camillocci, S. Morganti, A. Giordano, T. Scotognella, D. Rotili, V. Dini, F. Marini, I. Fratoddi, Y^{3+} embedded in polymeric nanoparticles: morphology, dimension and stability of composite colloidal system, *Colloids Surf. A Physicochem. Eng. Asp.* 532 (2017) 125–131, https://doi.org/10.1016/j.colsurfa.2017.05.082.

[13] I. Fratoddi, I. Venditti, C. Cametti, C. Palocci, L. Chronopoulou, M. Marino, F. Acconcia, M.V. Russo, Functional polymeric nanoparticles for dexamethasone loading and release, Colloids Surf. B 93 (2012) 59–66, https://doi.org/10.1016/j.colsurfb.2011.12.008.

[14] S. Jaiswal, P.K. Dutta, S. Kumar, J. Koh, S. Pandey, Methyl methacrylate modified chitosan: Synthesis, characterization and application in drug and gene delivery, *Carbohydr. Polym.* 211 (2019) 109–117, https://doi.org/10.1016/j.carbpol.2019.01.104.

[15] A. Abdollahi, H. Roghani-Mamaqani, M. Salami-Kalajahi, Morphology evolution of functionalized styrene and methyl methacrylate copolymer nanoparticles by one-step emulsifier-free emulsion polymerization, Eur. Polym. J. 133 (2020), 109790, https://doi.org/10.1016/j.eurpolymj.2020.109790.

[16] M. Jahanbakhshi, M. Shahrousvand, Preparation and characterization of cross-linked poly (vinyl alcohol-co-methyl methacrylate) colloidal nanoparticles from hydrolysis of poly (vinyl acetate-co-methyl methacrylate) as a promising cancer drug delivery system, Int. J. Polym. Mater. 91 (2022) 4037, https://doi.org/10.1080/00914037.2022.2155158.

[17] M. Mella, A. Tagliabue, G. Viscusi, G. Gorrasi, L. Izzo, How chemical structure and composition impact on the release of salt-like drugs from hydrophobic matrices: Variation of mechanism upon adding hydrophilic features to PMMA, Colloids Surf. A 646 (2022), 128878, https://doi.org/10.1016/j.colsurfa.2022.128878.

[18] S. Guo, Y. Liang, L. Liu, M. Yin, A. Wang, K. Sun, Y. Li, Y. Shi, Research on the fate of polymeric nanoparticles in the process of the intestinal absorption based on model nanoparticles with various characteristics: size, surface charge and pro-hydrophobics, J. Nanobiotechnol. 19 (2021) 32, https://doi.org/10.1186/s12951-021-00770-2.

[19] H. Kang, S. Rho, W.R. Stiles, S. Hu, Y. Baek, D.W. Hwang, S. Kashiwagi, M.S. Kim, H.S. Choi, Size-dependent EPR effect of polymeric nanoparticles on tumor targeting, Adv. Healthc. Mater. 9 (2020), 1901223, https://doi.org/10.1002/adhm.201901223.

[20] D. Cao, X. Zhang, M.D. Akabar, Y. Luo, H. Wu, X. Ke, T. Ci, Liposomal doxorubicin loaded PLGA-PEG-PLGA based thermogel for sustained local drug delivery for the treatment of breast cancer, Artif. Cells Nanomed. Biotechnol. 47 (2019) 181–191, https://doi.org/10.1080/21691401.2018.1548470.

[21] J.K. Tee, L.X. Yip, E.S. Tan, S. Santitewagun, A. Prasath, P.C. Ke, H.K. Ho, D. T. Leong, Nanoparticles' interactions with vasculature in diseases, Chem. Soc. Rev. 48 (2019) 5381–5407, https://doi.org/10.1039/C9CS00309F.

[22] Y. Tao, P. Ren, X. Yi, H. Zhou, S. Xiong, F. Ge, L. Chen, K. Yang, Self-assemble polymeric nanoparticle with GSH exhaustion for SPECT imaging–guided enhanced radioisotope therapy, Part. Part. Syst. Charact. 36 (2019), 1900018, https://doi.org/10.1002/ppsc.201900018.

[23] V. Perumal, P.M. Sivakumar, A. Zarrabi, S. Muthupandian, S. Vijayaraghavalu, K. Sahoo, A. Das, S. Das, S.S. Payyappilly, S. Das, Near infra-red polymeric nanoparticle based optical imaging in Cancer diagnosis, J. Photochem. Photobiol. 199 (2019), 111630, https://doi.org/10.1016/j.jphotobiol.2019.111630.

[24] N. Yamauchia, R. Yatabeb, H. Iinoa, M. Nagatsukaa, Y. Sogamec, M. Ogatad, Y. Kobayashia, Spontaneous immobilization of both a fluorescent dye and a functional sugar T during the fabrication of submicron-sized PMMA particles in an aqueous solution, Colloids Surf. A 604 (2020), 125299, https://doi.org/10.1016/j.colsurfa.2020.125299.

[25] L. Arms, D.W. Smith, J. Flynn, W. Palmer, A. Martin, A. Woldu, S. Hua, Advantages and limitations of current techniques for analyzing the biodistribution of nanoparticles, Front. Pharmacol. 9 (2018) 802, https://doi.org/10.3389/fphar.2018.00802.

[26] Z. Wang, O. Jacobson, R. Tian, R.C. Mease, D.O. Kiesewetter, G. Niu, M. Pomper, X. Chen, Radioligand therapy of prostate cancer with a long-lasting prostate-specific membrane antigen targeting agent ^{90}Y-DOTA-EB-MCG, Bioconjug. Chem. 29 (2018) 2309–2315, https://doi.org/10.1021/acs.bioconjchem.8b00292.

[27] P. Vo, T.A. Gooley, J.G. Rajendran, D.R. Fisher, J.J. Orozco, D.J. Green, A.K. Gopal, R. Haaf, M. Nartea, R. Storb, F.R. Appelbaum, O.W. Press, J.M. Pagel, B. M. Sandmaier, Yttrium-90-labeled anti-CD45 antibody followed by a reduced-intensity hematopoietic cell transplantation for patients with relapsed/refractory leukemia or myelodysplasia, Haematologica 105 (2020) 1731–1737, https://doi.org/10.3324/haematol.2019.229492.

[28] D. Rohan Jeyarajah, M.B. Majella Doyle, N. Joseph Espat, P.D. Hansen, D. A. Iannitti, J. Kim, T. Thambi-Pillai, B.C. Visser, Role of yttrium-90 selective internal radiation therapy in the treatment of liver-dominant metastatic colorectal cancer: an evidence-based expert consensus algorithm, J. Gastrointest. Oncol. 11 (2020) 443–460, https://doi.org/10.21037/jgo.2020.01.09.

[29] C. İçhedef, S. Teksöz, O. Çetin, B. Aydın, I. Sarıkavak, Y. Parlak, B.E. Bilgin, Design of ^{99m}Tc radiolabeled gemcitabine polymeric nanoparticles as drug delivery system and in vivo evaluation, Mater. Chem. Phys. 263 (2021) 124380, https://doi.org/10.1016/j.matchemphys.2021.124380.

[30] G. Gaikwad, N. Rohra, C. Kumar, S. Jadhav, H.D. Sarma, L. Borade, S. Chakraborty, S. Bhagwat, P. Dandekar, R. Jain, R. Chakravarty, A facile strategy for synthesis of a broad palette of intrinsically radiolabeled chitosan nanoparticles for potential use in cancer theranostics, J. Drug. Deliv. Sci. Technol. 63 (2021) 102485, https://doi.org/10.1016/j.jddst.2021.102485.

[31] C. Hwang, J.M. Kim, J.H. Kim, Influence of concentration, nanoparticle size, beam energy, and material on dose enhancement in radiation therapy, J. Radiat. Res 58 (2017) 405–411, https://doi.org/10.1093/jrr/rrx009.

[32] S.Y. Ong, C. Zhang, X. Dong, S.Q. Yao, Recent advances in polymeric nanoparticles for enhanced fluorescence and photoacoustic imaging, Angew. Chem. Int. Ed. 60 (2021) 17797–17809, https://doi.org/10.1002/anie.202101964.

[33] D. Cheng, Q. Xu, Separation distance dependent fluorescence enhancement of fluorescein isothiocyanate by silver nanoparticles, Chem. Commun. (2007) 248–250, https://doi.org/10.1039/B612401A.

[34] J. Li, G. Cui, S. Bi, X. Cui, Y. Li, Q. Duan, T. Kakuchi, Y. Chen, Eu^{3+}- and Tb[3+]-based coordination complexes of poly(n-isopropyl,n-methylacrylamide-stat-n,n-dimethylacrylamide) copolymer: synthesis, characterization and property, Polymers 14 (2022) 1815, https://doi.org/10.3390/polym14091815.

[35] R.T.F. Stepto, Dispersity in polymer science (IUPAC recommendation 2009), Polym. Int. 59 (2010) 23–24, https://doi.org/10.1002/pi.2748.

[36] S.A. Mohammad, S.Y. Zebary, Spectrophotometric assay of yttrium(III) with alizarin red S in the presence of cetyltrimethylammonium bromide -application to water samples, Raf. J. Sci. 27 (2018) 127–137, https://doi.org/10.33899/rjs.2018.145397.

[37] L. Shi, X. Wang, F. Zhao, H. Luan, Q. Tu, Z. Huang, H. Wang, H. Wang, In vitro evaluation of 5-aminolevulinic acid (ALA) loaded PLGA nanoparticles, Int. J. Nanomed. 8 (2013) 2669–2676, https://doi.org/10.2147/IJN.S45821.

[38] T.T. Puck, P.I. Marcus, Action of X-rays on mammalian cells, J. Exp. Med 103 (1956) 653–666, https://doi.org/10.1084/jem.103.5.653.

[39] H.-J. Yen, S.-H. Hsu, C.-L. Tsai, Cytotoxicity and immunological response of gold and silver nanoparticles of different sizes, Small 5 (2009) 1553–1561, https://doi.org/10.1002/smll.200900126.

[40] N. Gortany, G. Panahi, H. Ghafari, M. Shekari, M. Ghazi-Khansari, Foretinib Induces G2/M cell cycle arrest, apoptosis, and invasion in human glioblastoma cells through C-MET inhibition, Cancer Chemother. Pharmacol. 87 (2021) 827–842, https://doi.org/10.1007/s00280-021-04242-0.

[41] C.T. Singley, M. Solursh, The use of tannic acid for the ultrastructural visualization of hyaluronic acid, Histochemistry 65 (1980) 93–102, https://doi.org/10.1186/1477-7827-1-124.

[42] E. Pompili, V. Ciraci, S. Leone, V. De Franchis, P. Familiari, R. Matassa, G. Familiari, A.M. Tata, L. Fumagalli, C. Fabrizi, Thrombin regulates the ability of schwann cells to support neuritogenesis and to maintain the integrity of the nodes of ranvier, Eur. J. Histochem. 64 (2020) 3109, https://doi.org/10.4081/ejh.2020.3109.

[43] E. Montanari, N. Zoratto, L. Mosca, L. Cervoni, E. Lallana, R. Angelini, R. Matassa, T. Coviello, C. Di Meo, P. Matricardi, Halting hyaluronidase activity with hyaluronan-based nanohydrogels: development of versatile injectable formulations, Carbohydr. Polym. 221 (2019) 209–220, https://doi.org/10.1016/j.carbpol.2019.06.004.

[44] G. Reina, E. Tamburri, S. Orlanducci, S. Gay, R. Matassa, V. Guglielmotti, T. Lavecchia, M.L. Terranova, Nanocarbon surfaces for biomedicine, Biomatter 4 (2014), e28537, https://doi.org/10.4161/biom.28537.

[45] S. Derman, Caffeic acid phenethyl ester loaded PLGA nanoparticles: effect of various process parameters on reaction yield, encapsulation efficiency, and particle size, J. Nanomater 16 (2015) 318, https://doi.org/10.1155/2015/341848.

[46] S. Liu, M.C. Böhm, F. Müller-Plathe, Role of the interfacial area for structure and dynamics in polymer nanocomposites: molecular dynamics simulations of polystyrene with silica nanoparticles of different shapes, Mater. Res. Express 3 (2016), 105301, https://doi.org/10.1088/2053-1591/3/10/105301.

[47] B.J. Tickner, G.J. Stasiuk, S.B. Duckett, G. Angelovski, The use of yttrium in medical imaging and therapy: historical background and future perspectives, Chem. Soc. Rev. 49 (2020) 6169, https://doi.org/10.1039/C9CS00840C.

[48] N. Choudhury, P. De, Recent progress in pendant rhodamine-based polymeric sensors for the detection of copper, mercury and iron ions, J. Macromol. Sci. 58 (2021) 835–848, https://doi.org/10.1080/10601325.2021.1960172.

[49] B.L. Rivas, I. Moreno-Villoslada, Chelation properties of polymer complexes of poly (acrylic acid) with poly(acrylamide), and poly(acrylic acid) with poly(N,N-dimethylacrylamide), Macromol. Chem. Phys. 199 (1998) 1153–1160, https://doi.org/10.1002/(SICI)1521-3935(19980601)199:6<1153::AID-MACP1153>3.0.CO;2-R.

[50] U. Nakan, S. Bieerkehazhi, B. Tolkyn, G. Mun, M. Assanov, M. Nursultanov, R. Rakhmetullayeva, K. Toshtay, E. Negim, A. Ydyrys, Synthesis, characterization and antibacterial application of copolymers based on N,N-dimethyl acrylamide and acrylic acid, Materials 14 (2021) 6191, https://doi.org/10.3390/ma14206191.

[51] S. Bhattacharjee, DLS and zeta potential – what they are and what they are not, J. Control. Release 235 (2016) 337–351, https://doi.org/10.1016/j.jconrel.2016.06.017.

[52] R.J.M. Konings, A.S. Booij, High-temperature infrared spectroscopy of YCl3: the vibration spectrum, molecular structure and thermodynamic functions, J. Mol. Struct. 271 (1992) 183–190, https://doi.org/10.1016/0022-2860(92)80125-2.

[53] A. Shundo, K. Hori, D.P. Penaloza, K. Yoshihiro, M. Annaka, K. Tanaka, Nonsolvents-induced swelling of poly(methylmethacrylate) nanoparticles, Phys. Chem. Chem. Phys. 15 (2013) 16574, https://doi.org/10.1039/C3CP52673A.

[54] K. Kabiri, M.J. Zohuriaan-Mehr, H. Mirzadeh, M. Kheirabadi, Solvent-, ion- and pH-specific swelling of poly(2-acrylamido-2-methylpropane sulfonic acid) superabsorbing gels, J. Polym. Res. 17 (2010) 203–212, https://doi.org/10.1007/s10965-009-9306-7.

[55] T. López-León, E.L.S. Carvalho, B. Seijo, J.L. Ortega-Vinuesa, D. Bastos-González, Physicochemical characterization of chitosan nanoparticles: electrokinetic and stability behavior, J. Colloid Interface Sci. 283 (2005) 344–351, https://doi.org/10.1016/j.jcis.2004.08.186.

[56] Y. Hui, X. Yi, D. Wibowo, G. Yang, A.P.J. Middelberg, H. Gao, C.X. Zhao, Nanoparticle elasticity regulates phagocytosis and cancer cell uptake, Sci. Adv. 6 (2020) eaaz4316, https://doi.org/10.1126/sciadv.aaz4316.

[57] Bell, A.M.T.; Smith, A.J. Acta crystallographica. Section C, Crystal structure communications, 46, 6, 960–962, (1990). ⟨https://doi.org/10.1107/S0108270189009236⟩.